

Monte-Carlo simulations of neutron detector performance

Svyatoslav Mihailovich Tkachenko

Odessa, Ukraine

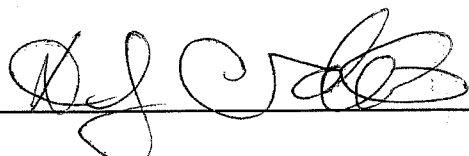
Specialist, Odessa State Polytechnical University, 1997

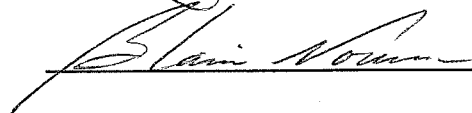
A Dissertation Presented to the Graduate Faculty of the University of
Virginia in Candidacy for the degree of Master of Science

Department of Physics

University of Virginia

August, 2004





Acknowledgements.

I want to thank my advisor Don Crabb for his academic and personal help without which I would not be able to reach this point. I thank all the people in Jefferson Lab who helped me in my research, especially, Bogdan Wojtsekhowski, Andrei Semenov, Pavel Degtyarenko, Vahe Mamyan. I thank Yelena Prok for her help and inspiration. I thank other members of the polarized target group who helped me at different stages of my research.

Abstract.

The form factors of the nucleons are important quantities giving information on the internal structure of nucleons and allowing for possibilities of testing for different theoretical models. The electric neutron form factor will be measured in the Jefferson Lab experiment E02-013 by measuring the asymmetry of the cross-section in double polarized, semi-exclusive ${}^3\vec{H}e(\vec{e}, e'n)pp$ scattering at high four-momentum transfers of $Q^2 = 1.3, 2.4$, and 3.4 (GeV/c)^2 . The neutron detection efficiency has been analyzed for the proposed neutron detector using the GEANT simulation package and MINUIT minimization package. The optimal iron converter thickness was analyzed and weighting coefficients for improving signal-to-noise ratio have been found.

The test run for the detector configuration similar to the one that will be used in the actual experiment was performed in 2003. The data from that run was used to check how well the simulations describe the actual data. Also, simulations checking how well the test run configuration can predict the actual experimental data were performed.

Contents

1	Introduction.	1
2	The double polarization method.	7
3	Experimental setup.	11
3.1	The CEBAF polarized beam.	11
3.2	The polarized ^3He target.	12
3.3	BigBite spectrometer.	14
3.3.1	BigBite detector stack.	15
3.3.2	The field clamp configuration for BigBite.	15
3.4	Neutron detector.	18
3.4.1	Structure of the neutron detector.	19
3.4.2	Parameters of the neutron detector.	21
3.4.3	Expected background rates and shielding.	22
3.4.4	Veto detector.	23
3.4.5	Veto efficiency for high energy protons.	24
3.4.6	Trigger and front-end electronics.	25
4	Proposed measurements.	27

4.1	Kinematics.	27
4.2	Asymmetry and rate estimates.	28
4.3	Error estimates.	30
4.3.1	Factors affecting extraction of G_E^N	31
5	Numerical simulations of neutron detection efficiency.	33
5.1	GEANT package.	33
5.2	Neutron detection.	34
5.3	Neutron detection efficiency.	36
5.4	Use of iron converters.	37
5.5	Test run.	38
5.6	Weighting coefficients for data.	41
6	Summary and conclusions.	48
A	Theoretical models for nucleon form factors.	50
A.1	Dipole parameterization.	50
A.2	Vector meson dominance models.	51
A.3	Gari-Krümpelmann model.	52
A.4	Quark models.	53
A.4.1	Bag models.	54
A.4.2	Quark model with hyperfine interactions.	56
A.4.3	Constituent quark models.	57
A.4.4	Diquark model.	58
A.5	Theoretical predictions on G_E^N	58

B	Helicity asymmetry in ${}^3\vec{He}(\vec{e}, e'n)$ and the ratio of G_E^N/G_M^N.	60
B.1	Nucleons in the nuclear medium.	60
B.2	${}^3\vec{He}$ as a neutron target.	62
B.3	Qualitative assessments of nuclear effects in the extraction of G_E^N/G_M^N from semi-exclusive $A(e, e'N)X$ reactions.	63
B.4	Preliminary results of the GEA calculation.	66
C	Quasi-elastic scattering at Q^2 of several $(GeV/c)^2$.	69
C.1	Selection of QES events.	70
C.2	Photo-production of charged pions.	75
C.3	QES from the protons in ${}^3\vec{He}$	76
C.4	Accidental background.	77
C.5	Analysis of the raw asymmetry and extraction of A_{perp}	77

Chapter 1

Introduction.

Discovery of the neutron by Chadwick [1] (1932) seemed to finish the compilation of the set of elementary particles that build matter. That set included the neutron, the proton and the electron. However, an uncertainty was brought into that rounded picture after only a couple of years. After the proton magnetic moment was measured in 1934 [2], its anomalous value suggested existence of internal structure in the proton. From there experiments measuring the root mean square radius of the proton charge started. Chambers and Hofstadter determined it to be 0.8 fm, using electron-proton scattering [3] (1956). Further high accuracy experiments determined it to be 0.81 fm [4, 5, 6, 7]. That was the end of the proton as a pointlike particle.

Frisch and Stern also measured the neutron magnetic moment [2] (1934), which turned out to be different from zero as it “should” have been according to the Dirac equation. This indicated that the neutron also has some substructure.

Quantitatively the structure of a nucleon is described by form factors. For example, the elastic differential cross-section of the electron scattering off a nucleon

is

$$\left(\frac{d\sigma}{d\Omega}\right) = \left(\frac{d\sigma}{d\Omega}\right)_{Mott} |F(q^2)|, \quad (1.1)$$

where

$\left(\frac{d\sigma}{d\Omega}\right)_{Mott}$ is the cross-section for a spinless point charge

q is the exchange 4-momentum

F is the “form factor”.

This “form factor” is a complicated quantity which contains electric and magnetic form factors of a nucleon (G_E and G_M). As their names indicate, they describe the nucleon charge and magnetic moment distributions. These quantities are essential in understanding nucleon structure. Moreover, they are ingredients in the analysis of processes involving electromagnetic interactions with complex nuclei.

Understanding nucleon structure is of immense importance in physics. The theory of strong interactions says that the valence structure of a nucleon is a bound state of three quarks. The electromagnetic current of a nucleon arises from the motion of three confined valence quarks and from the sea of virtual particles: q , \bar{q} , g . Since the nucleon is the simplest three-quark system, it’s a convenient laboratory for studying quark-gluon interactions.

The further interest in the neutron electric form factor was caused by recent surprising results on G_E^p , the electric form factor of the proton. Jefferson Lab experiments E93-027 and E99-007 indicated that the ratio G_E^p/G_M^p declines sharply as Q^2 increases [7, 8]. Thus, the electric and magnetic form factors of the proton behave differently from each other starting at $Q^2 \approx 1(\text{GeV}/c)^2$. The mechanisms causing this deviation could also be present in the neutron, supplying additional intrigue to the neutron form factors’ behavior.

Today, knowledge of proton form factors is more advanced than that of the neu-

tron. The electromagnetic form factors of the proton are fairly well-known from elastic electron-proton scattering up to Q^2 of about $10 (GeV/c)^2$. The situation with the neutron is much worse because of the absence of free neutron targets. Since the deuteron is the simplest and most weakly bound nuclear system the neutron electromagnetic form factors, historically, have been extracted from (unpolarized) electron-deuteron cross-section measurements. The magnetic form factor of the neutron G_M^N has been recently measured to better than 3.3 % [9, 10] at $Q^2 < 1.0 (GeV/c)^2$. However, since the neutron electric form factor G_E^N is very small, the removal of the dominating proton contribution and neutron magnetic form factor contribution to the deuteron cross-section introduces large uncertainties. Furthermore, to extract the neutron information, the wave functions have to be known and final state interactions (FSI), meson exchange currents (MEC), isobar current contribution amplitude (IC) and relativistic effects have to be taken into consideration. Thus, using electron-deuteron scattering leaves us with a rather poorly determined G_E^N form factor.

The aforementioned problems can be easily seen in Figure 1.1, which shows results for G_E^N determined in quasielastic e - d scattering. The uncertainties are rather large, and the result is compatible with both $G_E^N = 0$ and the Galster "parameterization" [12], an empirical fit to data on G_E^N obtained at lower values of Q^2 :

$$G_E^N = \frac{-\mu\tau}{1 + 5.6\tau} * G_D, \quad (1.2)$$

where G_D is the dipole form factor and $\tau = \frac{Q^2}{4m_N^2}$.

The problem can be solved by using the double polarization technique. By investigating spin observables, the interference between G_E^N and G_M^N enhances the sensitivity of these reactions to G_E^N . This was first discussed by Dombey in 1969 [13] and later by Akhiezer and Rekalo [14]. Arnold, Carson and Gross [15] suggested studying the

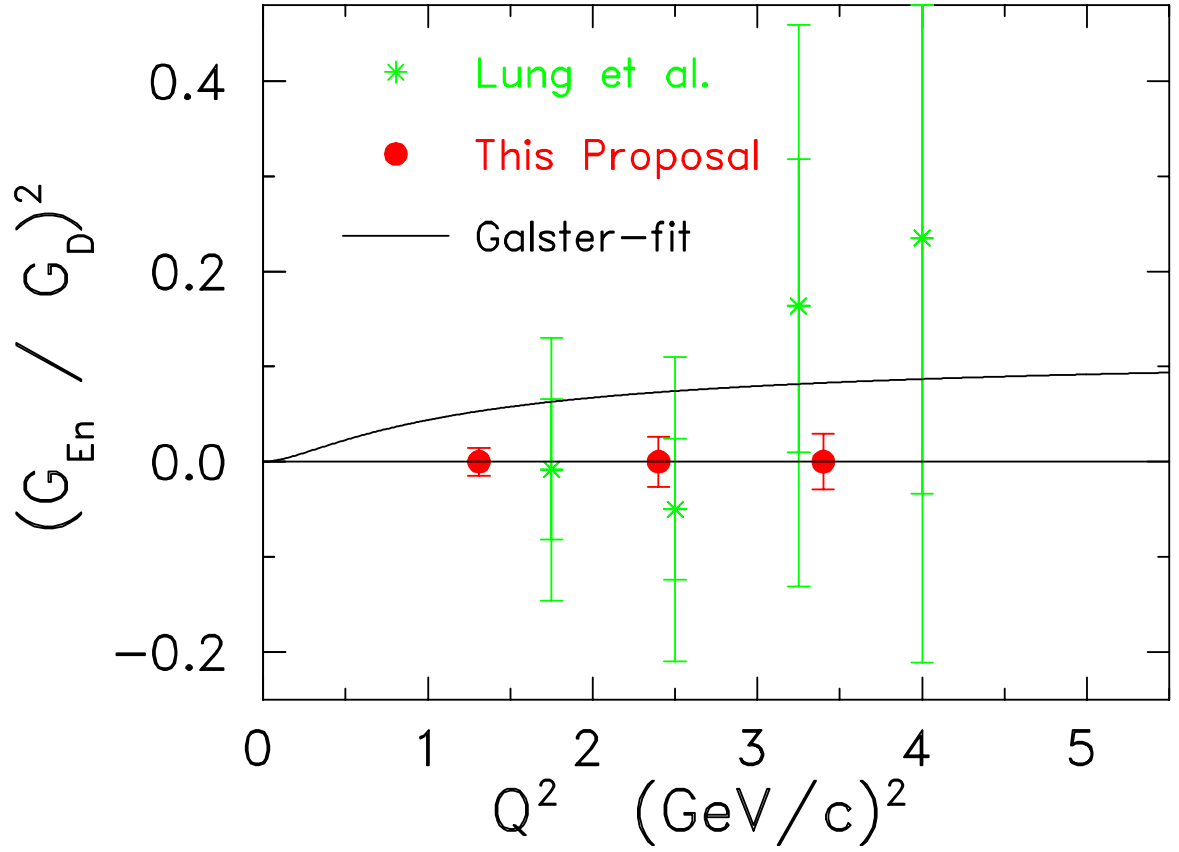


Figure 1.1: The ratio of the electric form factor and the dipole form factor as a function of Q^2 determined in quasi-elastic e-d scattering [11]. The solid line represents the Galster approximation [12] and the triangles show the statistical uncertainties expected in this experiment and show the values of Q^2 at which data will be taken.

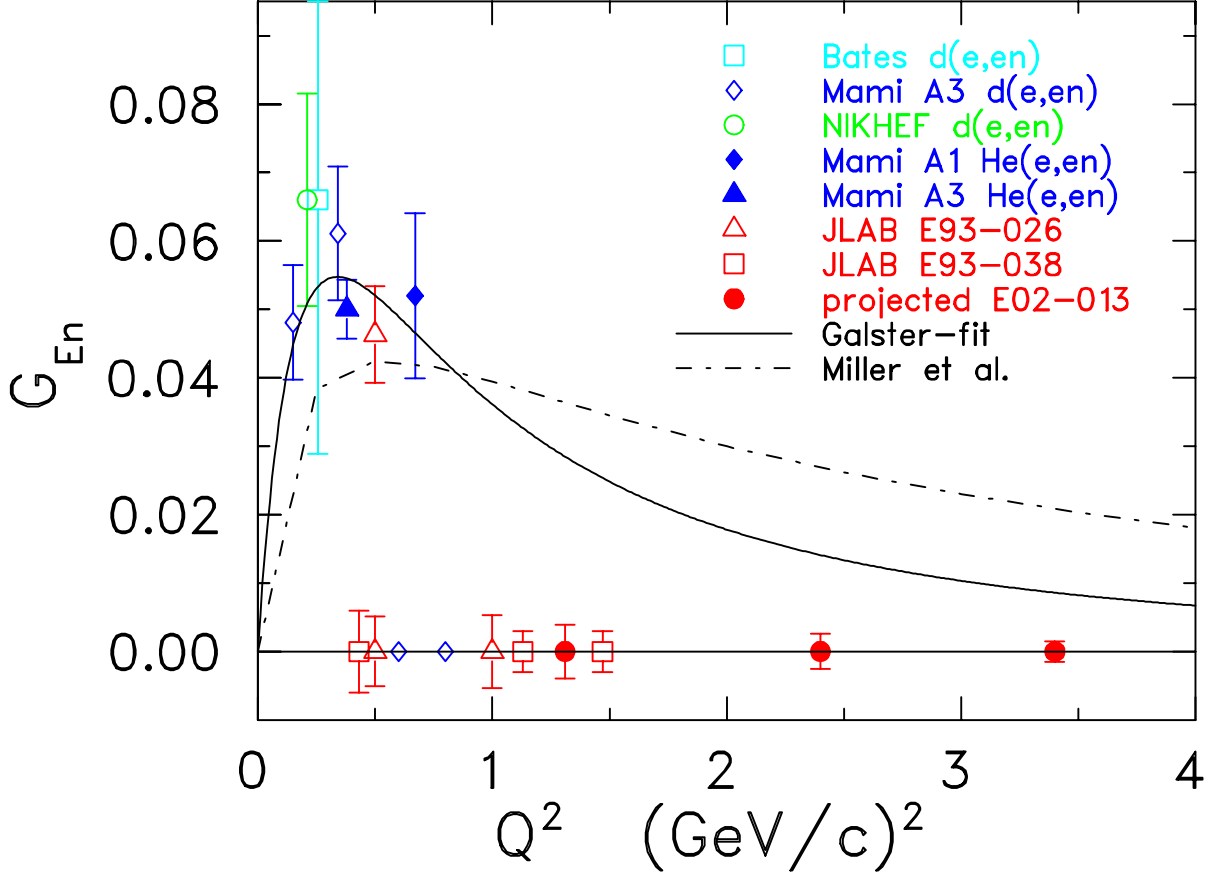


Figure 1.2: The published world data on G_E^N obtained in double polarization experiments [17, 18, 19, 20, 21, 22, 24, 25, 26]. For the experiments which have not published their results yet, only the expected uncertainty is plotted. Also shown are the projected error bars of E02-013.

$d(\vec{e}, e'\vec{n})p$ reaction to determine G_E^N . In 1984 Woloshin [16] suggested using a polarized ${}^3\text{He}$ target to measure G_E^N .

In the last ten years, a variety of double polarization experiments to measure G_E^N have been performed at different facilities: MIT-Bates, NIKHEF, MAMI, JLAB. As seen in Figure 1.2, the uncertainties are much smaller than those of e - d experiments, making the results much more encouraging and the double polarization technique very attractive.

The double polarization technique using a ${}^3\text{He}$ target will be used in the experiment under description. The proposed data points and their expected statistical uncertainties are shown in figure 1.1, next to the results from [11] and Galster fit. Points at momentum transfers of $Q^2 = 2.4$ and $Q^2 = 3.4(\text{GeV}/c)^2$ will give us the needed information on the G_E^N behavior at high energies and the point at $Q^2 = 1.3(\text{GeV}/c)^2$ will help to make a comparison with experimental data from other double polarization experiments and help study model dependency originating from the use of a ${}^3\text{He}$ target. The expected precision of data is comparable to the precision of the data on the proton, thus allowing a direct comparison of G_E^N and G_E^p . Also, due to the high momentum of the recoiling neutron a high neutron detection efficiency (of the order of 70%) is possible.

Chapter 2

The double polarization method.

In the Born approximation, the elastic electron-nucleon scattering cross-section (e - N) can be written as a sum of two parts: Σ , which corresponds to the unpolarized elastic cross-section $d\sigma/d\Omega_e$ and a polarized part Δ , which is only non-zero if the electron is longitudinally polarized (helicity $h = \pm 1$)

$$\sigma_h = \Sigma + h\Delta. \quad (2.1)$$

The asymmetry A_N for the e - N scattering cross-section is defined as

$$A_N = \frac{\sigma_+ - \sigma_-}{\sigma_+ + \sigma_-} = \frac{\Delta}{\Sigma}. \quad (2.2)$$

In the Born approximation the unpolarized e - N cross-section Σ for elastic scattering off a free nucleon at rest is

$$\Sigma = \sigma_M \left(\frac{G_E^2 + \tau G_M^2}{1 + \tau} + 2\tau G_M^2 \tan^2(\Theta/2) \right), \quad (2.3)$$

with

$$\sigma_M = 4\alpha^2 (\hbar c)^2 \frac{E_f^2}{Q^4} \cos^2(\Theta/2) \frac{E_f}{E_i} \quad (2.4)$$

being the Mott cross-section, which describes the scattering from a pointlike target.

In the above equations E_i (E_f) is the electron's initial (final) energy, m_N is the mass

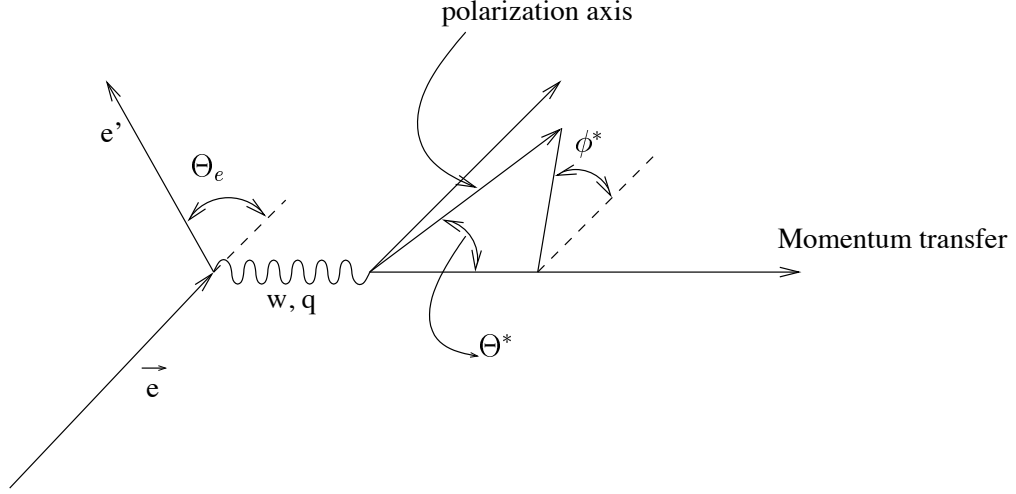


Figure 2.1: The kinematics of electron scattering from polarized target

of the nucleon, Q^2 is the negative square of the four-momentum transfer, G_E^N and G_M^N are the electric and magnetic Sachs form factors of the nucleon respectively. The polarized part is given by

$$\Delta = -2\sigma_M \sqrt{\frac{\tau}{1+\tau}} \tan(\Theta/2) \left(\sqrt{\tau(1+(1+\tau)\tan^2(\Theta/2))} \cos \Theta^* G_M^2 + \sin \Theta^* \cos \phi^* G_M G_E \right), \quad (2.5)$$

where Θ^* is the polar angle and ϕ^* is the azimuthal angle of the target polarization in the laboratory frame with respect to the direction of the momentum transfer (see Fig.2.1).

The measured experimental asymmetry for the ${}^3\overline{H}e(\vec{e}, e'n)$ reaction is reduced compared to the ideal $\vec{n}(\vec{e}, e'n)$ reaction because of the finite polarization of the electron beam P_e , the finite polarization of the neutrons P_n in the 3He target, the dilution D from atoms other than 3He in the target, and the dilution $V = (1 + N/S)^{-1}$ of events originating from random coincidences and reactions other than quasielastic scattering, where N/S is the noise-to-signal ratio. At JLab (Jefferson Lab), a beam

polarization of $P_e = 0.75$ is routinely achieved. The polarized ${}^3\overrightarrow{He}$ target has been operated at an average value of $P_{He} = 0.40$ during recent polarized target experiments. The total spin of 3He is mainly carried by the neutron, so a polarized 3He target represents an effective polarized neutron target. As it has been shown, even for a 100% polarized 3He nucleus the neutron itself has polarization of 0.86 ± 0.02 . Additionally, the protons are not completely unpolarized, but have a polarization of 0.028 ± 0.004 . So the polarization of the neutron P_n is only 86% of the polarization of 3He . Also the presence of nitrogen in the target cell leads to $D = 0.94$ and background events lead to $V = 0.91$.

The measured asymmetry from the neutron can be expressed as follows:

$$A_{exp} = P_e * P_n * D * V * A_{phys} \quad (2.6)$$

with

$$A_{phys} = - \frac{2\sqrt{\tau(\tau+1)}\tan(\Theta/2)G_E^N G_M^N \sin\Theta^* \cos\phi^*}{(G_E^N)^2 + (G_M^N)^2(\tau + 2\tau(1+\tau)\tan^2(\Theta/2))} - \frac{2\tau\sqrt{1+\tau+(1+\tau)^2\tan^2(\Theta/2)}\tan(\Theta/2)(G_M^N)^2 \cos\Theta^*}{(G_E^N)^2 + (G_M^N)^2(\tau + 2\tau(1+\tau)\tan^2(\Theta/2))}. \quad (2.7)$$

By aligning the target spin perpendicular to the momentum transfer, one gets the perpendicular asymmetry

$$A_{perp} = -\frac{G_E^N}{G_M^N} \cdot \frac{2\sqrt{\tau(\tau+1)}\tan(\Theta/2)}{((G_E^N/G_M^N)^2 + (\tau + 2\tau(1+\tau)\tan^2(\Theta/2)))}. \quad (2.8)$$

Because $(G_E^N/G_M^N)^2$ is small compared to the second term of the denominator in our kinematics, G_E^N is nearly proportional to A_{perp} . To extract G_E^N out of this ratio, knowledge of G_M^N is necessary. Fortunately, G_M^N is, or soon will be, sufficiently well known. The recent experiment E94-017 at JLab was a measurement of G_M^N up to $Q^2 = 4.8(GeV/c)^2$ which will provide very accurate data [34]. The large acceptance

non-focusing spectrometer (BigBite) will be used in the electron arm and the neutron detector constructed for this experiment will be used in the neutron arm (see chapter 3). Due to their large acceptance, the perpendicular spin alignment can only be made for part of the acceptance, and longitudinal contributions to the asymmetry have to be taken into account:

$$A_{long} = -\frac{2\tau\sqrt{1+\tau+(1+\tau)^2\tan^2(\Theta/2)}\tan(\Theta/2)}{(G_E^N/G_M^N)^2+(\tau+2\tau(1+\tau)\tan^2(\Theta/2))}. \quad (2.9)$$

Nevertheless, these contributions are small, and depend - to the first order - only on kinematics, not on the value of G_E^N itself. Together with the ability to reconstruct the scattering angles and the momentum transfer, these corrections are under control.

The above discussion described scattering from a free nucleon. The general case of scattering from a bound nucleon was also analyzed by Donnelly [35]. Additional components, which appear in the cross-section, are nulled when the cross-section is integrated over the azimuthal angle of the nucleon momentum relative to the direction of the momentum transfer and the electron scattering plane. The Fermi motion of the nucleon inside the nucleus leads to kinematical effects on A_{perp} . Because of the dependance of the γ^*n cross-section on the internal momentum of the nucleon the average energy of the scattering is reduced as compared to the free nucleon at rest. As a result a non-zero value of A_{long} appears.

Chapter 3

Experimental setup.

This experiment will study the scattering of polarized electrons from polarized ^3He (see Fig.3.1). The scattered electron will be detected in the BigBite spectrometer, while a new, large solid angle scintillator array, matched to the BigBite acceptance, will be used to detect the recoiling neutron. The enhanced target cells will be used to ensure optimal performance during the experiment. The neutron detector will use new and existing neutron bars from several collaborating institutions; a large number of them have already come from UVA.

3.1 The CEBAF polarized beam.

The beam of $12\ \mu\text{A}$ with 75% polarization was assumed in the rate calculations. Currents in excess of $12\ \mu\text{A}$ with beam polarization as high as 75% already have been delivered over long periods of time using the strained GaAs source at Jefferson Lab [36]. The beam polarization will be measured with the Hall A Moeller polarimeter, which is able to measure it with a systematic uncertainty of 3%. This uncertainty can be improved by calibrating the Moeller polarimeter against the Compton polarimeter,

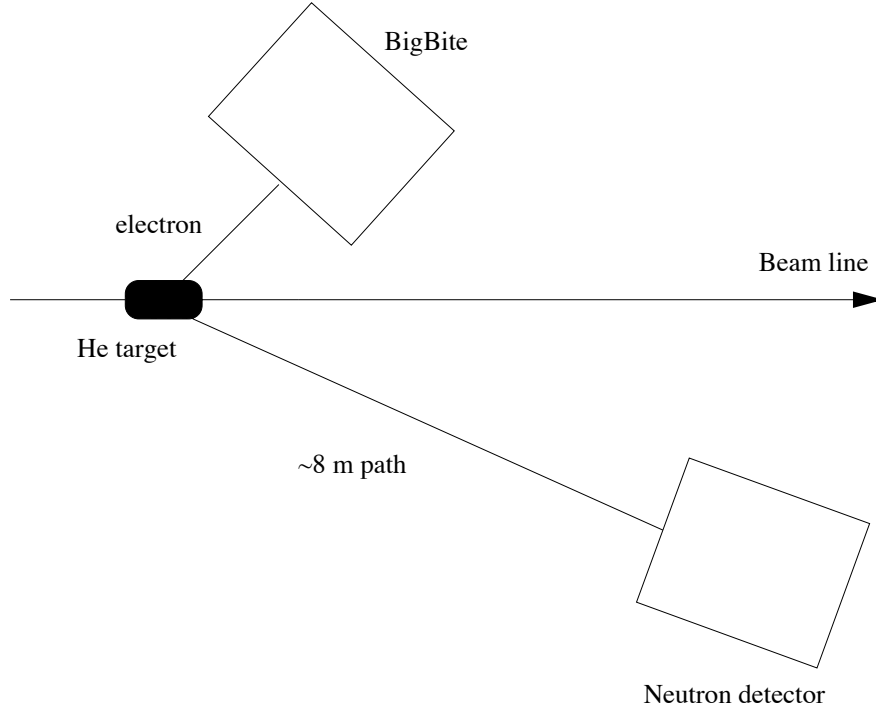


Figure 3.1: Layout of the experimental setup

which itself has a systematic uncertainty of only 1.4%, but cannot be used directly to measure the beam polarization because of the low current of $12 \mu A$.

3.2 The polarized 3He target.

The experiment will utilize the polarized 3He target that has been constructed and successfully employed for a series of experiments in Hall A [37]. The target is based on the principle of spin exchange between optically pumped Rb vapor and 3He gas. Polarizations of 40-50% can be achieved this way. The polarized luminosity reaches 10^{36} with $15 \mu A$ beam. With no free polarized neutron targets available, the polarized 3He target provides an excellent approximation due to the spin of the two protons in 3He being almost all paired in opposite directions.

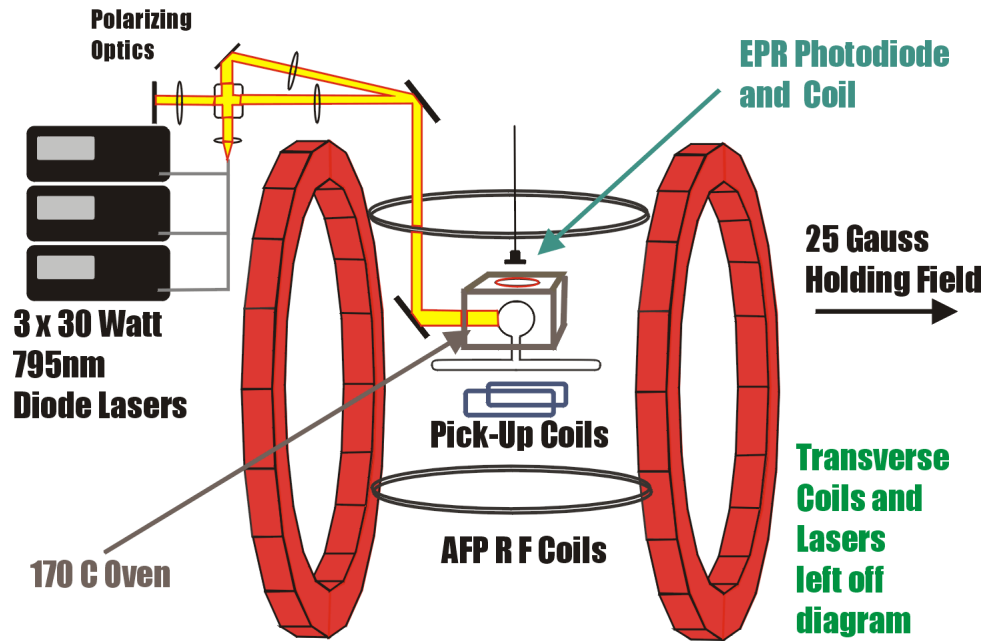


Figure 3.2: Hall A polarized ^3He target.

At the heart of the target system is sealed glass target cell, pictured toward the center of Fig. 3.2, which contains approximately 10 atmospheres of ^3He , around 70 Torr of nitrogen and a few droplets of Rb. The cell has two chambers: an upper “pumping chamber” in which the optical pumping and spin exchange take place, and a lower “target chamber” through which the electron beam passes during the experiment. The chambers are connected by a transfer tube that allows the ^3He to diffuse back and forth between the two chambers with a time scale that is short compared to the time it takes (24-28 hours) to polarize a cell. The magnetic holding field is roughly 25 Gauss, and is supplied by two large sets of coils that are roughly in a Helmholtz configuration.

In the experiment E02-013, polarizations higher than the aforementioned 40-50% are expected. Possible polarization suppression factors include the evolution of im-

purities in the glass during operation conditions, which is addressed with the help of a coating technique based on sol-gel technology [38]. The interior surface of the cell is coated with a layer of glass that is free of impurities. Higher polarizations can be achieved, or at least, a greater success rate can be demonstrated for the fabrication of target cells with good performance characteristics. Also, magnetic field gradients from the BigBite magnet can interfere with the polarization. The gradients can be suppressed using a field clamp.

3.3 BigBite spectrometer.

Scattered electrons will be detected in the BigBite spectrometer [39] (Fig.3.3). BigBite is a non-focusing large momentum and angular acceptance spectrometer that was originally designed and built for use at the internal target facility of the AmPS ring at NIKHEF [40, 41]. The spectrometer consists of a single dipole magnet (maximum magnetic field 1.2 Tesla) and a detection system. The original detector package included two sets of multi-wire drift chambers (MWDC), a plastic scintillator and an aerogel Cerenkov detector. To cope with the high rates possible at JLab, it was decided to upgrade the detector package. This was needed by a few experiments in Hall A. The single large plastic scintillator is replaced by a segmented two-layer array of plastic scintillators, with the first δE layer consisting of thin (3 mm) counters and the second E layer consisting of thick (3 cm) counters. Each plane is segmented into 24 elements which will be read out on both sides by fast PMTs. There are also plans to replace the original MWDCs with multi-wire proportional chamber to improve the rate capability. MWDCs will be employed for this experiment because of their higher resolution. The momenta of the scattered electrons in this experiment will be

between 1200-1500 MeV/c. In order to make their field integral through the BigBite dipole as large as possible, the magnet will be run at its maximum field of 1.2 T. To minimize field gradients at the position of the target, a field clamp will be added to the spectrometer.

3.3.1 BigBite detector stack.

The particle tracking will be performed by the existing MWDCs with an upgraded DAQ. A 3 cm thick iron plate will be placed behind the second MWDC to protect the trigger plane from low energy (less than 150 MeV) protons. The trigger will be formed by two segmented planes of scintillator counters. A lead glass shower detector will be placed behind the trigger planes. The shower counter will allow the measurement of the electron's energy with a 10% resolution, which is sufficient to suppress background from other particles. It's planned to use the shower detector from the high resolution spectrometer (HRS) which has an active area of $75 \times 240 \text{ cm}^2$.

3.3.2 The field clamp configuration for BigBite.

The operation of the ${}^3\overrightarrow{He}$ target requires small magnetic field gradients (the gradient averaged over the target volume must be below 30 mG/cm). The BigBite spectrometer was used at NIKHEF with an internal ${}^3\overrightarrow{He}$ target [42]. It was found that the field clamp covering only the coils was sufficient to keep the gradient below 30 mG/cm for dipole excitations up to 0.9 Tesla. Above this level the fringe field of the saturated iron yoke created larger gradients.

It's planned to put a field clamp which will isolate the BigBite dipole from the target. The idea is to put an iron plate perpendicular to the magnetic holding field. An identical plate will be located on the opposite side to cancel first order distortions

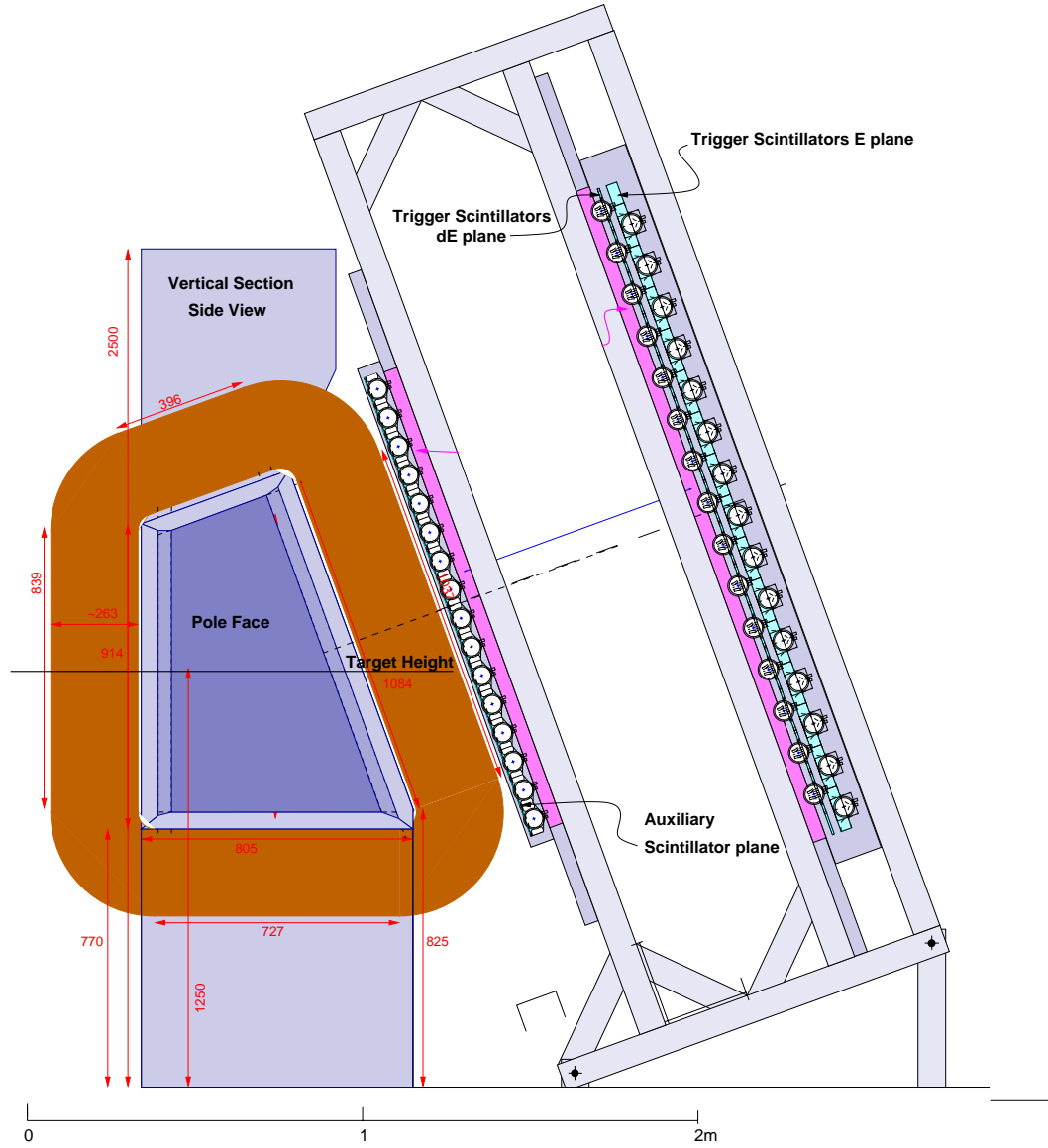


Figure 3.3: The BigBite spectrometer, side view.

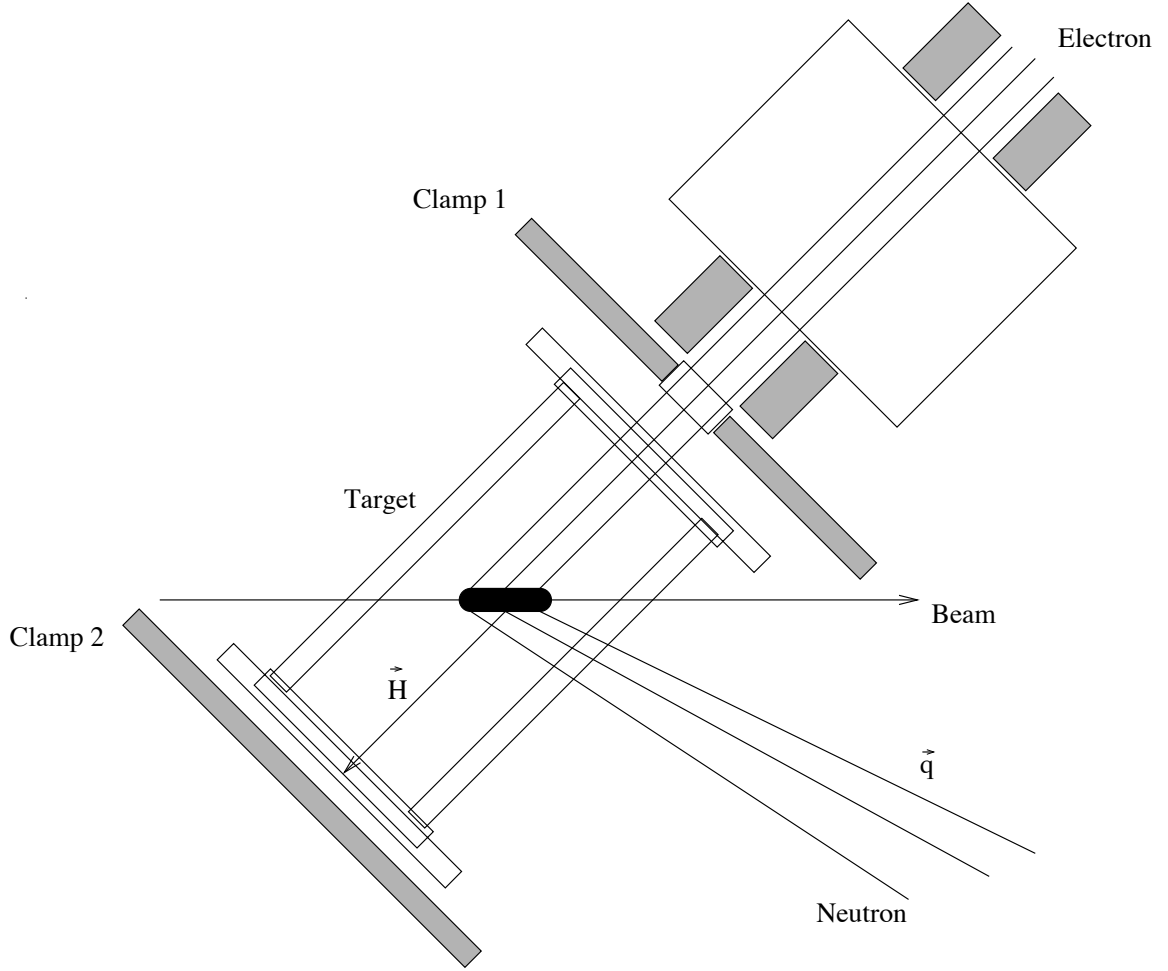


Figure 3.4: The concept of the field clamp configuration for the BigBite dipole.

of the field induced by the first plate.

A complete 3-D calculation with the MAFIA package [43] was performed for a configuration which includes the coils and the clamps from Fig. 3.4, but not BigBite [38]. The field gradient was found to be below 20 mG/cm in the target volume.

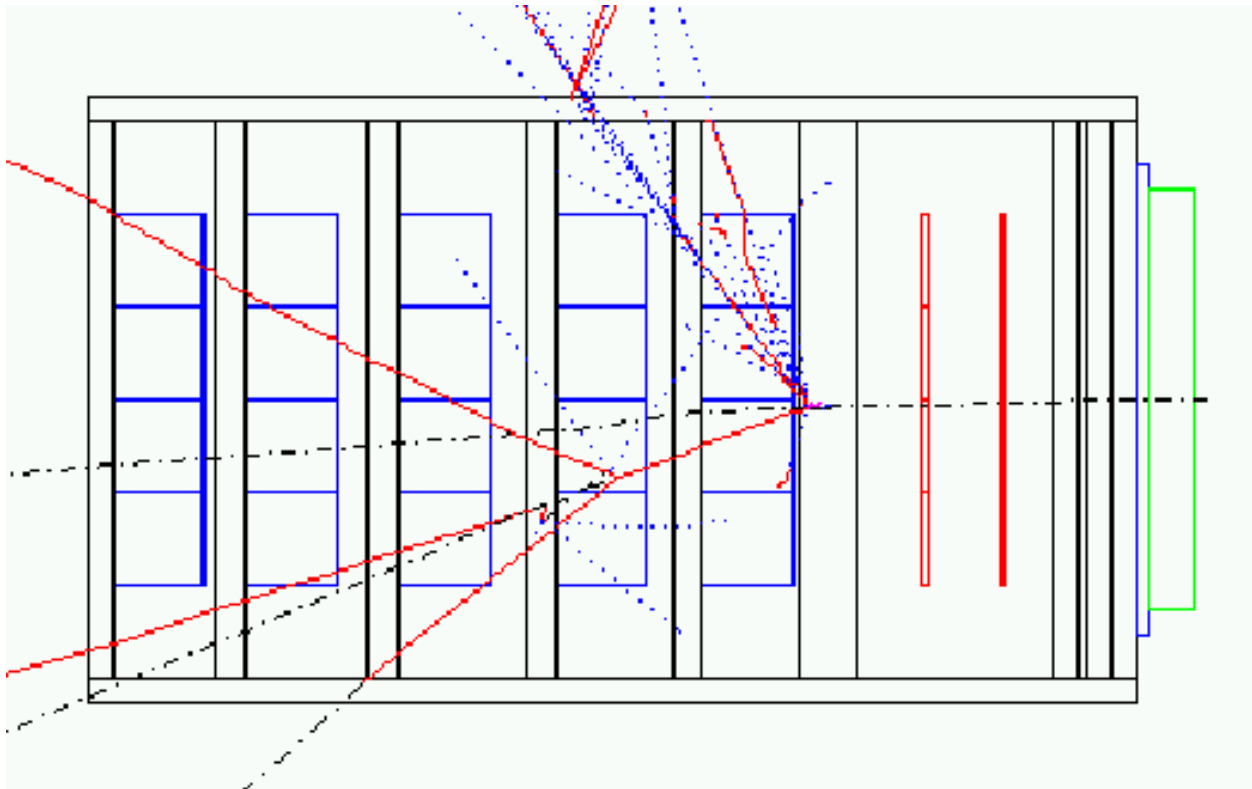


Figure 3.5: The neutron detector for the test run with one neutron event, side view. Scintillator bars are blue; veto detectors are red; the layer of lead bricks is shown green, with an aluminum sheet behind it; passive iron converters are shown in black between the scintillator bars.

3.4 Neutron detector.

The design of the neutron detector for this experiment¹ is based on many considerations, including detector acceptance and efficiency, background suppression, and availability of the counters and electronics. There are several considerations that are specific to the conditions of the experiment on hand:

¹For more on the detector see Chapter 5

- The large kinetic energy of the neutron leads to the possibility of using high thresholds in the trigger and for off-line analysis.
- The relatively low luminosity for the polarized ^3He target simplifies the background situation.
- The high velocity of the neutrons requires the largest possible distance from the target.

The required acceptance of the neutron detector was evaluated in two steps. First the acceptance for exact elastic scattering was found from the Monte-Carlo (MC) simulations (*cf.* Fig.3.6). In the second step the size was increased in each direction to ensure the acceptance of all events with p_{mperp}^2 of at least 150 MeV/c. For the $Q^2 = 3.4(\text{GeV}/c)^2$ point the horizontal and vertical size of the detector was increased by ± 47 cm in both directions. For the lower Q^2 points the distance between the target and the neutron detector will be decreased.

The structure of the detector is presented in the following section. The trigger logic presented in the last section will allow for a high hardware threshold, the detector efficiency considerations are presented in Chapter 5.

3.4.1 Structure of the neutron detector.

This experiment focuses on large momentum transfers, where the recoiling neutrons have kinetic energies of 0.7 GeV, 1.3 GeV, and 1.8 GeV corresponding to Q^2 of 1.3 $(\text{GeV}/c)^2$, 2.4 $(\text{GeV}/c)^2$ and 3.4 $(\text{GeV}/c)^2$ respectively. Such large energies allow a high detection efficiency for neutrons, and at the same time they allow the application of relatively high thresholds to suppress background from low energy particles.

²The transverse component of the missing momentum of the neutron, for more see Appendix B

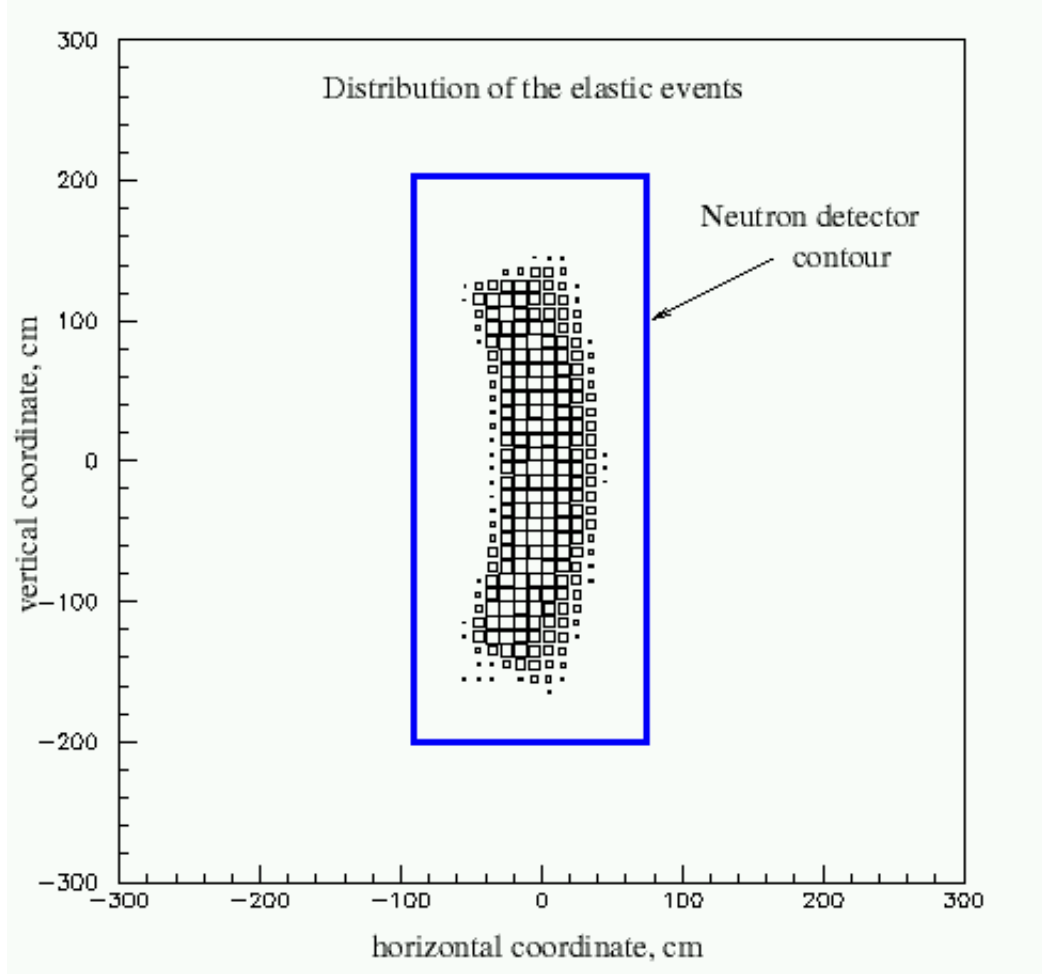


Figure 3.6: Required dimensions of the neutron detector.

Initially, the detector layout, consisting of five layers of scintillator bars was proposed with most of the counters having $10 \times 10 \times 160 \text{ cm}^3$ dimensions [38]; this was changed later (see chapter 5). Each neutron bar is equipped with two photomultipliers, one on each end. In front of each detector there is an iron converter which is 2.75 cm thick (A preliminary consideration, this is the thickness used in the test run; see chapter 5 for more). The front of the detector is covered by two layers of veto detectors protected by a 2 cm thick iron plate and a 2 in thick layer of lead. Between the veto counters and the front layer of the neutron bars, there is an additional 3.75 cm thick iron plate

to provide additional shielding from low energy particles.

3.4.2 Parameters of the neutron detector.

The solid angle of the neutron detector is approximately 100 msr at a distance of 8 m from the target. The aspect ratio is 1:2:5. With such geometry, the acceptance of the neutron detector matches the acceptance of the BigBite spectrometer, for events up to $p_{\text{mperp}} \approx 150 \text{ MeV}/c$.

The time resolution is expected to be 0.3 ns (σ). This value has been routinely achieved with the counters under consideration [44]. At a distance of 8 m, the 0.3 ns time resolution leads to a neutron momentum resolution of 250 MeV/c for the neutron momentum of 2.58 GeV/c.

The horizontal intersection point of the neutron with the neutron detector will be determined utilizing the time difference between the times it takes light to reach the two phototubes located on the ends of each neutron detector, while the vertical intersection point will be identified using the segmentation of the neutron detector. Based on Monte-Carlo simulations and experience from other experiments [44, 26] using the same counters, a resolution of 5 cm in both directions is expected. Some sample values of detection efficiency versus threshold for the proposed configuration are presented in Table 3.1. These were checked later using a GCalor hadronic shower simulation package (see Table 5.1) for a 50 MeV threshold. The position resolution presented in this table was found from the ratio of amplitudes of the signals on PMTs located on the opposite sides of the scintillator bars, which is another method to determine the position of the shower.

P_n , GeV/c	A_{thr} , MeVee	50	100	150
0.80	$\eta, \%$	30	15	5
1.35	$\eta, \%$	56	40	27
	σ_{pos} , cm	9.2	8.2	7.2
2.00	$\eta, \%$	73	62	51
	σ_{pos} , cm	8.2	8.2	7.9
2.58	$\eta, \%$	79	71	60
	σ_{pos} , cm	8.5	7.9	7.5

Table 3.1: Neutron detection efficiency η and position resolution σ_{pos} versus threshold for $P_n = 0.80, 1.35, 2.00$, and 2.58 GeV/c.

3.4.3 Expected background rates and shielding.

In this experiment the $12 \mu A$ beam will pass through a 40 cm long 3He target. The total thickness of the glass entrance and exit windows is $240 \mu m$. Therefore, a luminosity of $5 \cdot 10^{36}$ electron-nucleon/s/ cm^2 is used for background estimates. Because the diameter of the target cell is only 2 cm and because both detectors are located at relatively large angles (25° and 50°) it will be possible to collimate the entrance and exit windows without significant loss of useful target length. Such a collimation will reduce the background rate in each arm (the neutron detector and BigBite) by a factor of two. However, in the following analysis the effect of these collimators will not be taken into account, so the actual background can be up to two times smaller than estimated.

The beam also passes through two Be vacuum windows (total thickness 0.5 mm) and two Al windows at the target chamber (total thickness 0.25 mm). The total amount of material in the windows is about $160 mg/cm^2$. These windows cannot

contribute to the rate in BigBite because of its limited acceptance. It is also planned to install thick lead collimators around each of these windows in the direction of the neutron detector. In the following analysis leaks through the last collimators were not included.

An MC simulation [45], which was confirmed in several measurements [46], allows the prediction of yields of different particles. The MC simulation was done for the incident beam energy of 3.5 GeV on the Hall A polarized ^3He target, which includes the ^3He gas, two 0.12 mm glass windows and 1.3 mm side walls. The online rejection of the background will be done by setting a threshold of 50 MeVee for the sum of PMT signals. Pions and protons contribute most to the trigger rate of 500 kHz (for a threshold of 50 MeVee). In the analysis, the use of information from the veto counters and of high thresholds on the value of the total signal in the neutron counters (150 MeV for the highest Q^2 point) allows the reduction of the rate to the level of 10 kHz, where protons and pions will contribute evenly.

The expected trigger rate on the electron arm is about 200 kHz. The coincidence time window will be 25 ns. A rate of 500 kHz for the hardware neutron trigger will lead to an acceptable DAQ rate of 2.5 kHz.

While the detector is shielded from the direct flux of particles produced at the target by a 2 cm iron plate, the installation of similar shielding on the other side should reduce the rates on PMTs even further.

3.4.4 Veto detector.

Plastic scintillator counters will be used to distinguish neutrons from protons. The flux of low energy electrons, which will dominate the rate in the veto paddles, can also be found from Monte-Carlo simulations. The rate of electrons with energies above

10 MeV in one paddle of the veto detector (2.5 msr) is estimated to be 23 MHz; for electrons with energies above 30 MeV it will be 1.5 MHz. With an energy threshold of 0.5 MeV in the discriminator of the veto detector, which is protected by 2 cm of iron, the probability of detecting an electron with an incident energy of 10 MeV is 1.2%. The same parameter for electrons with 30 MeV of incident energy is of the order of 10%. As a result, the expected rate in one veto counter can be estimated to be below 0.5 MHz. Such a rate coupled with a 25 ns dead time per pulse leads to a total electronics dead time of the veto detector on the level of 1.25%. A further reduction of this dead time would require another set of veto detectors oriented vertically.

3.4.5 Veto efficiency for high energy protons.

The reaction ${}^3\text{He}(e, e'p)$ has a few times higher rate than the reaction ${}^3\text{He}(e, e'n)$. The standard way to distinguish between these processes is based on the use of plastic veto counters. The p,n charge exchange reaction, which can take place in the material between the target and the veto detector, can compromise the effectiveness of this approach. In this experiment the materials between the ${}^3\text{He}$ target and the veto detector are: the glass of the target cell (0.7 g/cm^2), the windows of the scattering chamber (0.1 g/cm^2), the air on the 8 meter long flight path to the detector (1 g/cm^2), and the 2 cm protection iron plate (15.6 g/cm^2).

From Monte-Carlo simulations it was found that the 2 cm iron wall, protecting veto detectors from the direct flux of particles from the target in front of the veto detectors, will introduce a 0.5% loss in detection efficiency for 2.6 GeV/c protons. Although the probability of hadronic interactions is about 15%, thus reducing the number of protons penetrating the wall, secondary particles produced in these interactions will give signals in the detectors. The upper limit for effects from other materials is

1% based on the total probability of hadron interactions and the acceptance of the neutron detector.

3.4.6 Trigger and front-end electronics.

The logic of the summing electronics is presented in Fig. 3.7. The individual PMT signal will be sent to a customized fan-in-fan-out/discriminator-sum unit. This unit will accept up to sixteen signals from PMTs, produce logic pulses for the timing measurement of each PMT, provide analog signals for ADC analysis and output the summing signal S. Because most of the hadronic shower is contained in the area 40 cm wide, the sum of two signals like S1 and S2 will be used and sent to a discriminator D1. The groups overlap to avoid any loss of detection efficiency. The output signal of the coincidence between D1 and the meantimer MT1 will be used as a clean and accurate timing signal. Nineteen such signals will be summed again in a logical OR to make the neutron trigger. The use of a separate sum for the left and right groups and meantimers allows the reduction of the walk of the neutron trigger signal (a difference in the time two exactly coincident signals might be registered, due, for example, to a different risetime) and enables the use of 25 ns gates for the coincidence with the electron arm. The veto counters are not used in trigger logic; however, they have the same type of TDC and ADC connections. The signals from all PMTs will be digitized by ADCs and TDCs.

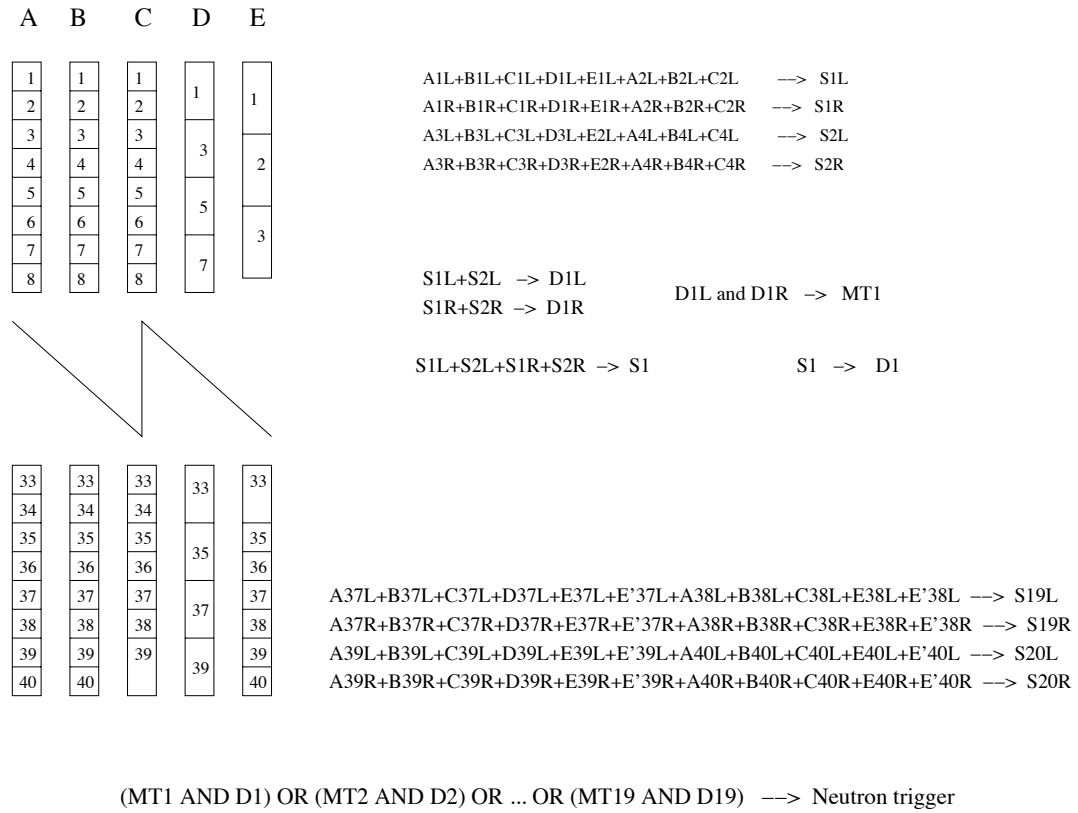


Figure 3.7: Layout of the neutron detector trigger logic.

Chapter 4

Proposed measurements.

4.1 Kinematics.

To choose which is the best combination of beam energy and scattering angle to measure G_E^N for a given Q^2 , one has to evaluate the figure-of-merit (FOM). In our case the FOM is given by

$$FOM = R(\Theta)/(\partial(G_E^N/G_M^N)/\partial A_{perp})^2, \quad (4.1)$$

where $R(\Theta)$ is the counting rate, which itself is proportional to the cross-section times the effective target length and the acceptance of the particular spectrometers used. The FOM of the experiment is approximately proportional to $E_f^2/E_i^2 = (E_i - Q^2/2M)^2/E_i^2$, where E_i (E_f) is the initial (final) energy of the electron. Thus, for a given Q^2 , the FOM increases for higher beam energies, which corresponds to detecting an electron at lower scattering angles. The variation of G_E^N does not change the general behavior of the FOM. The difference between the FOM for the HRS and for the BigBite reflects the different solid angle and the different transverse acceptances of the two devices. The maximum momentum for electrons in the BigBite spectrometer

Table 4.1: The three proposed kinematics.

Q^2 (GeV/c) ²	E_i GeV	Θ_e deg	p_e GeV/c	Θ_n deg	p_n GeV/c	T_n GeV
1.31	1.644	54.6	0.95	35.2	1.34	0.70
2.40	2.444	54.6	1.17	28.3	2.01	1.28
3.40	3.244	50.6	1.43	25.4	2.58	1.81

is 1.5 GeV/c [39], which limits the scattering angles to values above 50° and the beam energy to roughly 3.3 GeV for a Q^2 of 3.4 (GeV/c)². Although the HRS spectrometer would allow us to go to more forward angles, the FOM would nevertheless be smaller than with the BigBite spectrometer due to its smaller solid angle. The other two kinematics were chosen so that the beam energy can be changed by changing the number of passes in the accelerator. Table 4.1 summarizes the proposed kinematics.

4.2 Asymmetry and rate estimates.

The asymmetry A_{phys} in e-n scattering is related to the measured asymmetry $A_{exp} = (N_+ - N_-)/N$ via the equation

$$A_{phys} = \frac{A_{exp}}{V \cdot D \cdot P_e \cdot P_n}, \quad (4.2)$$

where $D=0.94$ and $V=0.91$ are dilution factors, P_e is the polarization of the beam, and $P_n = 0.86P_{He}$ is the polarization of the neutron. In the following estimates we assume $P_e = 0.75$ and $P_{He} = 0.40$, both of which are values which have been achieved during recent experiments in Hall A using the polarized 3He target.

The following rate estimates are based on scattering from a free neutron. Experiments to study color transparency [47] have shown that, in a wide range of nuclei,

the quasi-elastic scattering cross-section is reduced by a factor of $c \cdot A^{\alpha(Q^2)}$, where c is unity within uncertainty; A is the mass number of the nucleus; and $\alpha = 0.25$ for the momentum transfers proposed in this experiment, leading to a reduction of the cross-section by a factor of 0.75 for ${}^3\text{He}$. Radiative corrections further reduce the number of useful events. The correction factors for these effects are estimated to be between 0.82 and 0.85. To distinguish the quasi-elastic scattering process from others, tight cuts on the missing momentum have to be applied. We expect to reduce the number of counts by a factor of 0.66 due to these cuts. As already pointed out, the asymmetry will be studied as a function of p_{mperp} . Therefore, the results have to be analyzed in separate bins, each of which must include enough statistics to obtain the desired statistical precision. We are planning to get events in three different p_{mperp} bins. The rates and asymmetries we expect, using these assumptions, are shown in Table 4.2.

Q^2 (GeV/c) ²	rate Hz	A_{exp}	G_E^N (Galster)
1.3	13.8	-0.0295	0.0284
2.4	1.49	-0.0260	0.0141
3.4	0.45	-0.0233	0.0086

Table 4.2: Rate estimates for E02-013 [38]. We assume a target polarization P_{He} of 40%, a beam polarization P_e of 75%, dilution factors $D=0.94$ and $V=0.91$, an average beam current of $12\mu A$, an effective target length of $25\text{ cm}/\sin\Theta_e$, and a solid angle of 76 msr for the electron arm. Furthermore, this rate is calculated assuming that G_E^N follows the Galster approximation and that we detect the neutrons with an efficiency of 60%.

4.3 Error estimates.

The uncertainty δA can be expressed as

$$\left(\frac{\delta A_{phys}}{A_{phys}}\right)^2 = \left(\frac{\delta A_{exp}}{A_{exp}}\right)^2 + \left(\frac{\delta P_e}{P_e}\right)^2 + \left(\frac{\delta P_n}{P_n}\right)^2 + \left(\frac{\delta D}{D}\right)^2 + \left(\frac{\delta V}{V}\right)^2. \quad (4.3)$$

The beam polarization in Hall A can be measured with the Compton and the Moeller polarimeter to better than 3%. Both polarimeters are standard equipment in Hall A. The polarization of 3He can be measured with an uncertainty of 4%, the polarization of neutrons in 3He is known to 2%. The combined uncertainty in D and V is estimated to be 5%. For small asymmetries, the statistical uncertainty δA_{exp} can be approximated as $\delta A_{exp} = 1/\sqrt{N}$. The corrections to the asymmetry due to contributions from A_{long} lead to an additional uncertainty of 1%. To extract G_E^N from the measured A_{phys} , equation (2.7) has to be evaluated. Investigating the error propagation in this equation, taking into account the complete denominator, but neglecting the longitudinal part, leads to

$$\left(\frac{\Delta G_{G_E^N}}{G_{G_E^N}}\right)^2 = \left(\frac{\delta G_{G_M^N}}{G_{G_M^N}}\right)^2 + \left[\left(\frac{\delta A_{phys}}{A_{phys}}\right)^2 + \left(\frac{\delta f_{nucl}}{f_{nucl}}\right)^2\right] C^2 \left(1 - \frac{1}{R}\right)^2 (G_E^N)^{-2} \quad (4.4)$$

with

$$C = 2\sqrt{\tau(1+\tau)} \tan(\Theta/2) \frac{G_M^N}{2A_{phys}} \quad (4.5)$$

and

$$R = \sqrt{1 - 4\tau[1 + 2(1 + \tau) \tan^2(\Theta/2)] \left(\frac{A_{phys}}{2\sqrt{\tau(1+\tau)} \tan(\Theta/2)}\right)^2}. \quad (4.6)$$

Knowledge of G_M^N is mandatory. Hall B experiment E94-107 will provide data for G_M^N with an accuracy better than 5%. As discussed before, we expect the correction factor f_{nucl} for nuclear effects to be 0.85-1.0, and the corresponding systematic error to be below 5%. Table 4.3 summarizes the various contributions to the total error for the example of the highest Q^2 point.

Quantity	Expected value	rel. uncertainty
statistical error in raw asymmetry A_{exp}	-0.0233	13.4%
beam polarization P_e	0.75	3%
target polarization P_{He}	0.40	3%
neutron polarization P_n	$0.86P_{He}$	2%
dilution factor D	0.94	3%
dilution factor V	0.91	4%
correction factor for A_{long} components	0.94	1%
G_M^N	0.057	5%
nuclear correction factor	0.85-1.0	5%
statistical error in G_E^N		13.8%
systematic error in G_E^N		10.4%

Table 4.3: The various contributions to the total error in G_E^N for the data point at $Q^2=3.4(GeV/c)^2$.

4.3.1 Factors affecting extraction of G_E^N .

There are nuclear medium effects, which may interfere with extracting G_E^N from the experiment. First of all, it is now clear that structure functions depend on the size of the nucleus (EMC effect). This effect is possible to control because of the small values of missing momentum and the fact that the measured asymmetry involves ratios of form factors which are not as sensitive to the EMC effect as the form factors themselves. Color transparency (CT) is another effect that could potentially cause a problem, but previous experiments [47] didn't show any significant influence of CT in the studied region of momenta.

Some other nuclear effects would involve: off-shell effects, meson exchange effects,

delta isobar contribution, final state interactions. See Appendix B for a more detailed discussion of these effects.

Chapter 5

Numerical simulations of neutron detection efficiency.

The neutron detector consists of multiple layers of plastic scintillators, separated by iron converters which increase the probability of neutron interactions in the detector. Similar setups have been used lately [48] and have proven to enhance neutron detection efficiency. The optimal thickness of the converters is the subject of Monte-Carlo simulations using the GEANT package, which are described later. Also the possibility of using weighting coefficients for data from different layers in order to improve the signal-to-background noise ratio is considered and results of simulations are presented. Comparison of the actual data from the test run with the simulation is included.

5.1 GEANT package.

GEANT [49] is a system of detector description and simulation tools, that can help

- design and optimize the detectors;
- develop and test the reconstruction and analysis programs;
- interpret the experimental data.

This package was developed in CERN (1974) and belongs to the CERN program library. The hadronic shower simulations are assisted by GHEISHA, FLUKA or GCALOR packages.

GEANT version 3 was used in the simulations. This is a much more advanced program than its 1974 predecessor. It is a rather universal program that is capable of describing a variety of particle interactions over a big range of energies. The GEANT 3 code is based on Fortran. The newer version (GEANT 4), based on C++, is becoming more and more popular these days.

5.2 Neutron detection.

A charged particle passing through matter ionizes and excites molecules of the material. The ionization and excitation are the basis of the particle detection and measurement. It is possible to use similar methods for the detection and measurement of uncharged particles, like neutrons, since they produce secondary charged particles when passing through matter.

Different methods of detecting radiation have been developed over years. In some of them (dosimeters) only the integrated effect of several ionizing radiations is measured, in some (track visualization instruments) trajectories of particles are recorded, in some (counters) individual ionizing particles are detected and recorded. The counters are the most common tool of detecting radiation nowadays since they provide

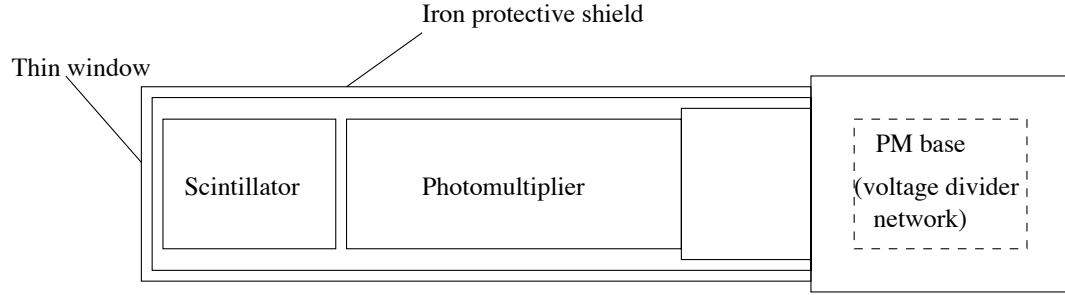


Figure 5.1: Schematic diagram of a scintillation counter.

most information on particles' behavior.

The scintillation counter is one of the most often and widely used particle detection devices in nuclear and particle physics these days. It uses the fact that some materials emit light when hit by a nuclear particle or radiation, the process known as scintillation. This small flash of light can be amplified and converted into electrical signals by a photomultiplier. These signals can be then analyzed and counted electronically to give information concerning incident radiation.

The scintillation detector (see Fig. 5.1) consists of a scintillating material which is optically coupled to a photomultiplier either directly or via a light guide. As radiation passes through the scintillator, it excites the atoms and molecules making up the scintillator causing light to be emitted. The light is transmitted to a photomultiplier where it is converted into a current of photoelectrons which is then amplified by an electron-multiplier system.

The signal provided by the scintillator is sensitive to energy; is of short duration, thus allowing higher counting rates.

Neutrons interact primarily with the nuclei of the absorber material, rather than with atomic electrons. Being uncharged massive particles they easily penetrate electron clouds and collide with the nuclei. The interactions of neutrons with nuclei are

of two types, scattering and absorption. In the former the neutron collides with a nucleus and a fraction of the neutron energy is transferred to the recoil nucleus. In the latter the neutron is absorbed by the nucleus. The excited product nucleus may emit γ radiation or a nuclear reaction may occur in which heavy charged particles are emitted. We are interested in high energy neutrons, whose detection relies mainly on detecting the recoil proton in the (n,p) scattering processes.

5.3 Neutron detection efficiency.

Two types of efficiency are generally referred to when discussing radiation detection: absolute efficiency and intrinsic efficiency [51]. The absolute efficiency is the fraction of events emitted by the source which are actually registered by the detector. In my work I was concerned with the other kind, intrinsic efficiency which is the fraction of events actually hitting the detector that are registered. In general, this efficiency depends on the interaction cross-sections of the incident radiation on the detector medium. Thus, the intrinsic efficiency is a function of the type of radiation, its energy and the detector material. For charged particles, the intrinsic efficiency is usually high, since charged particles almost always produce some ionization. The problem of efficiency is more important for neutral particles like neutrons as they must first interact to create secondary charged particles. These interactions are much rarer and there is no guarantee of good detection efficiency of neutral particles. The dimensions of the detector become important as sufficient mass must be present to provide a good probability of interaction. The efficiency of the detection is also influenced by the scintillator material, which can absorb part of the light that it emitted (self-absorption). This was taken into account in numerical simulations. Also, the

detector bars which will be used in the experiment were tested using cosmic rays and demonstrated good light propagation properties (the light absorption length was of the order of six meters, which is very good for a scintillator bar with a length of 160 cm).

5.4 Use of iron converters.

Detection of high energy neutrons poses the significant problem of combining high efficiency of detection with very good energy resolution. To achieve high detection efficiency, we need a detector to have a total thickness of several nuclear interaction lengths. Since the interaction length $\lambda \approx 80$ cm for high energy neutrons in typical scintillator materials, such thicknesses would pose problems for time of flight measurements (since the interaction could happen anywhere inside the detector) and, hence, for energy resolution measurements:

$$\delta T_n/T_n = \gamma(\gamma + 1) [(\delta S/S)^2 + (\delta T/T)^2]^{-1/2}, \quad (5.1)$$

where $\delta T_n/T_n$ is the energy resolution, γ is the Lorentz factor, S is the measured flight path, T is the flight time, δS and δT are the respective resolutions.

Thus, to achieve relatively good time resolution a thinner detector is desirable, but it lowers the detection efficiency. This can be fixed by using passive converters, where neutron-induced showers start and which are later detected in the scintillators. Indeed, studies show [48] that passive converters can greatly improve the detection efficiency. The small interaction length versus the cost of the material is the decisive factor in what material is used for the converter. The obvious candidates are iron and lead; iron is the best choice due to its interaction length being comparable to that of lead and to its cost being lower.

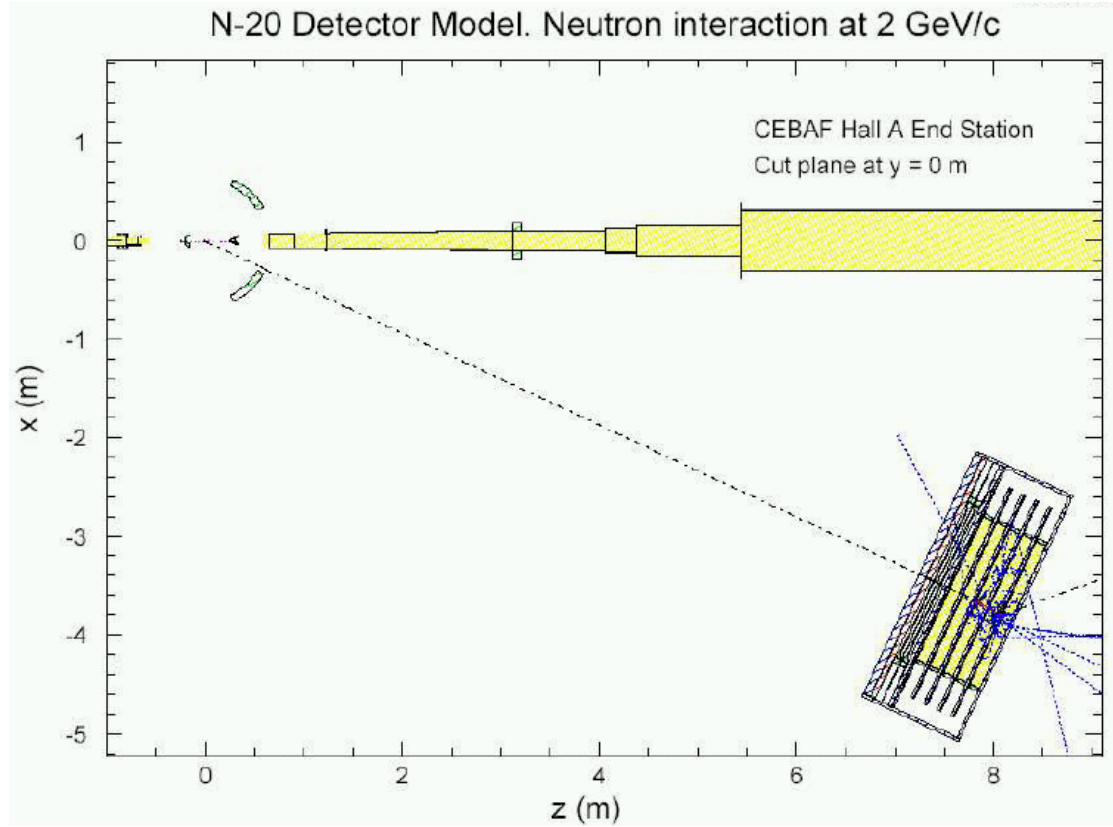


Figure 5.2: The top view of the test experiment configuration. Only the neutron arm is used.

5.5 Test run.

A test run of the setup was performed in 2003. The run used only the neutron arm as shown in the Figure 5.2. The neutron detector, while having features similar to the actual run detector, had only four layers of neutron detector bars, oriented vertically (see Fig. 5.3), as opposed to the forty projected in the actual experiment (see Fig. 5.4). The main purposes of the test run were to check the background loads on the DAQ system and to compare them to the acceptable rate (see section 3.4.3), and to test and optimize the detector design.

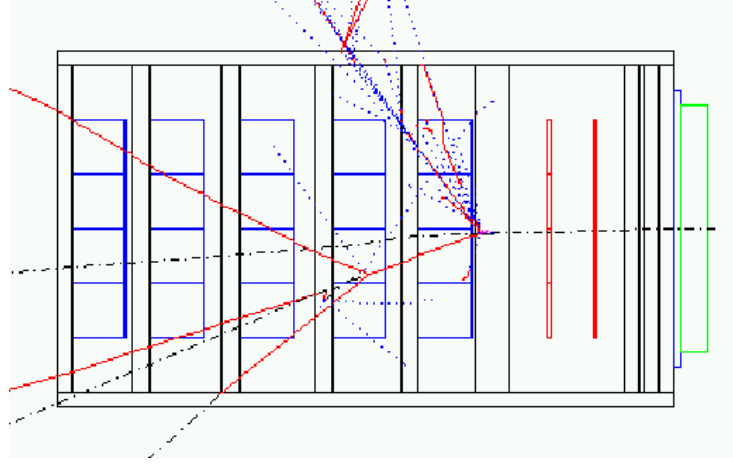


Figure 5.3: The neutron detector for the test run with one neutron event, side view.

For the test run configuration, Monte-Carlo simulations of the dependence of the detection efficiency on the thickness of converters were performed using the GEANT simulation package. Results for reasonable thicknesses of the converters can be seen from Table 5.1. As seen from the simulation results, the projected peak in detection efficiency is at about 5-7 cm thickness of the iron converters. The shape of the detector signal from the simulations is shown in figure 5.5. The simulation was performed for neutrons with the initial momenta $p_{ini} = 2.58 \text{ GeV}/c$.

Event exclusion by veto was not included in this simulation so as to facilitate the best possible comparison with the test run. Still, an accurate comparison is not possible due to the aforementioned absence of veto signals and the fact that only the neutron arm was used in the experiment: that is, the coincidence events between the neutron and electron arms were not present. Still, as one can see, comparing Fig. 5.6 to Fig. 5.5; the experimental signal is close in shape to the simulated one, providing a good level of confidence as for the possibility of accurate simulation of the real data.

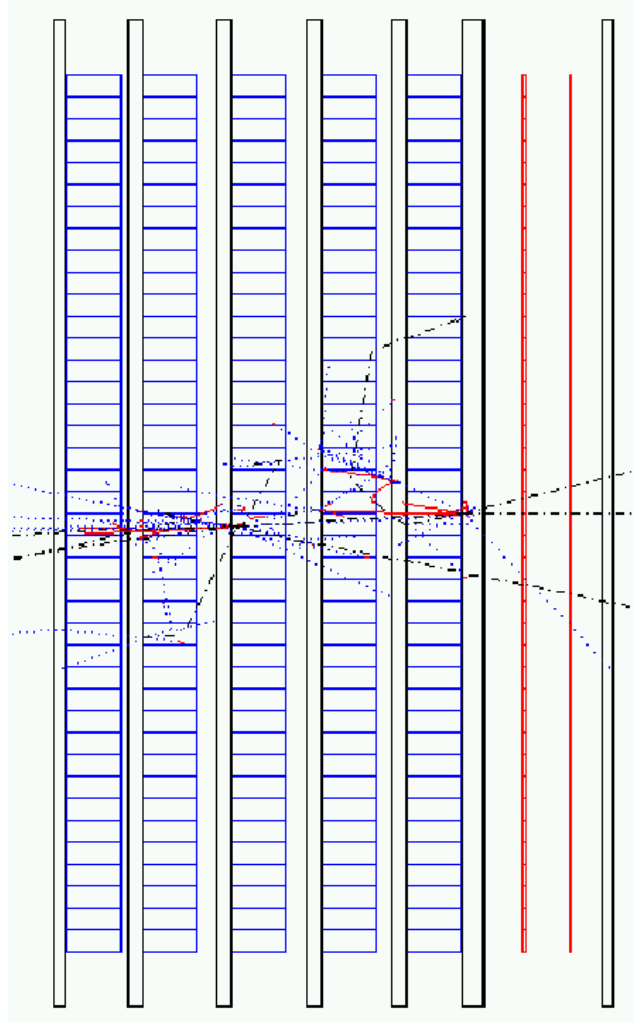


Figure 5.4: The neutron detector for E02-013 with one neutron event, side view.

The experiment will have 40 layers of neutron detectors in the vertical plane. The simulation on how well the four detector configuration can approximate the final configuration was performed. The result can be seen in figure 5.7, where the signals from all 40 detectors, central four and central eight were plotted. As one can see, the energy output from the central four detector bars is shifted to the lower energies, since some energy “leaks out” to the neighboring detector bars, while the energy output of eight detectors is already a good approximation of the full forty detector setup. The

Thickness of one converter,cm	Efficiency, %
0.75	67
1.75	73
2.75	78
3.75	82
4.75	83
5.75	85
6.75	87
7.75	82
8.75	82

Table 5.1: Thickness of iron converters versus detection efficiency.

neutrons in the aforementioned simulations were sent into one spot in the middle of the detector setup. This turned out to be a very good approximation for the actual run where different neutrons hit different spots of the detector (see figure 5.8).

5.6 Weighting coefficients for data.

The next step of simulations was to analyze the data from the experimental neutron detector configuration. The simulations were performed at the initial neutron momenta of 2.58 GeV/c and 0.8 GeV/c, where 2.58 GeV/c events were considered to be the actual signal and 0.8 GeV/c events were used as a background noise. The configuration of the neutron detector was slightly changed to incorporate the latest design solutions, which were made possible by the larger number of detector bars contributed by participating institutions. The number of layers became seven, with

15×5cm detectors in the first three layers and 10×10 cm detectors in the other four layers. The simulation was performed for a smaller number of detector bars vertically, since, as it can be seen from Fig. 5.7, this approximates the full configuration really well, while keeping the computer time to a reasonably low amount (see fig.5.9). The neutrons were sent into the detector, spread around in such a way that they covered the second layer of the detector bars. This time, the selection of events by veto was included. If the sum of energies collected in all veto detectors in an event was greater than 0.5 MeV, the event was excluded. The additional selection was introduced by the energy threshold, imitating the threshold in the actual experiment. In the simulation under consideration it was set to 50 MeV: that is, if an event produced an energy output less than 50 MeV (sum over all the detector bars), the event was excluded.

The rest of the events from the simulation were saved and further analyzed using the MINUIT minimization package. Energies produced by different layers at the two momenta (sums of energies from all the neutron bars in one layer) were summed with weighting coefficients and the results were combined in such a way that the “0.8 GeV/c” energy was minimized by the same coefficients that maximize the “2.58 GeV/c” energy. The idea behind this is that with proper weighting coefficients the signal-to-noise ratio will be maximized, thus increasing the usefulness of the data. The challenging task was to find the proper functional form facilitating this minimization process. After trying several of those, it was found that the simple ratio=noise/signal is functionally good enough.

The starting values of coefficients were 1/7, so that the sum over all layers reproduced the total energy collected in the whole detector. After running the data through MINUIT, the best coefficients were found and the summary of those is given in Table 5.2. The statistical errors are unreliable due to Minuit not handling errors

Layer number	Weighting coefficient
1	$0.63 \cdot 10^{-1} \pm 0.35$
2	$0.12 \cdot 10^{-1} \pm 0.28 \cdot 10^{-2}$
3	$0.50 \cdot 10^{-1} \pm 0.95 \cdot 10^{-1}$
4	$0.43 \cdot 10^{-1} \pm 0.11$
5	$0.26 \cdot 10^{-1} \pm 0.51 \cdot 10^{-1}$
6	$0.70 \pm 0.73 \cdot 10^{-3}$
7	$0.13 \cdot 10^{-1} \pm 0.99 \cdot 10^{-2}$

Table 5.2: Weighting coefficients for layers of scintillator bars in the neutron detector.

well except for some special cases. However, the mean values are reliable.

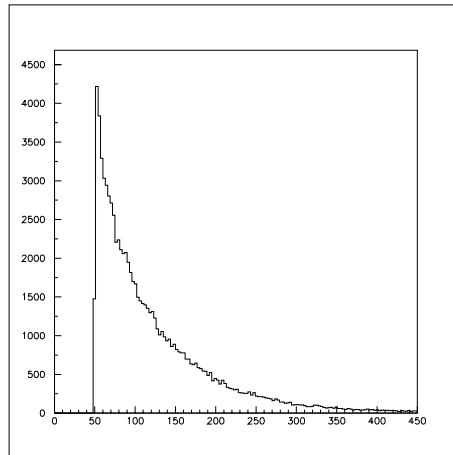


Figure 5.5: The neutron detector response from the numerical simulations.

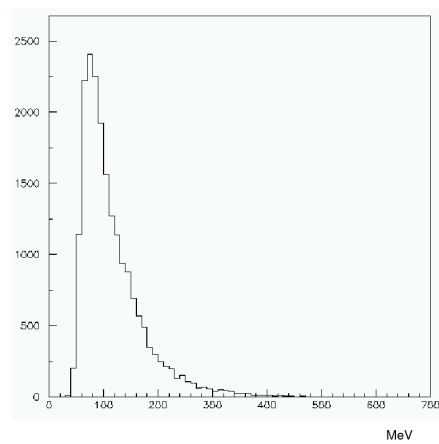


Figure 5.6: The neutron detector response from the test experiment.

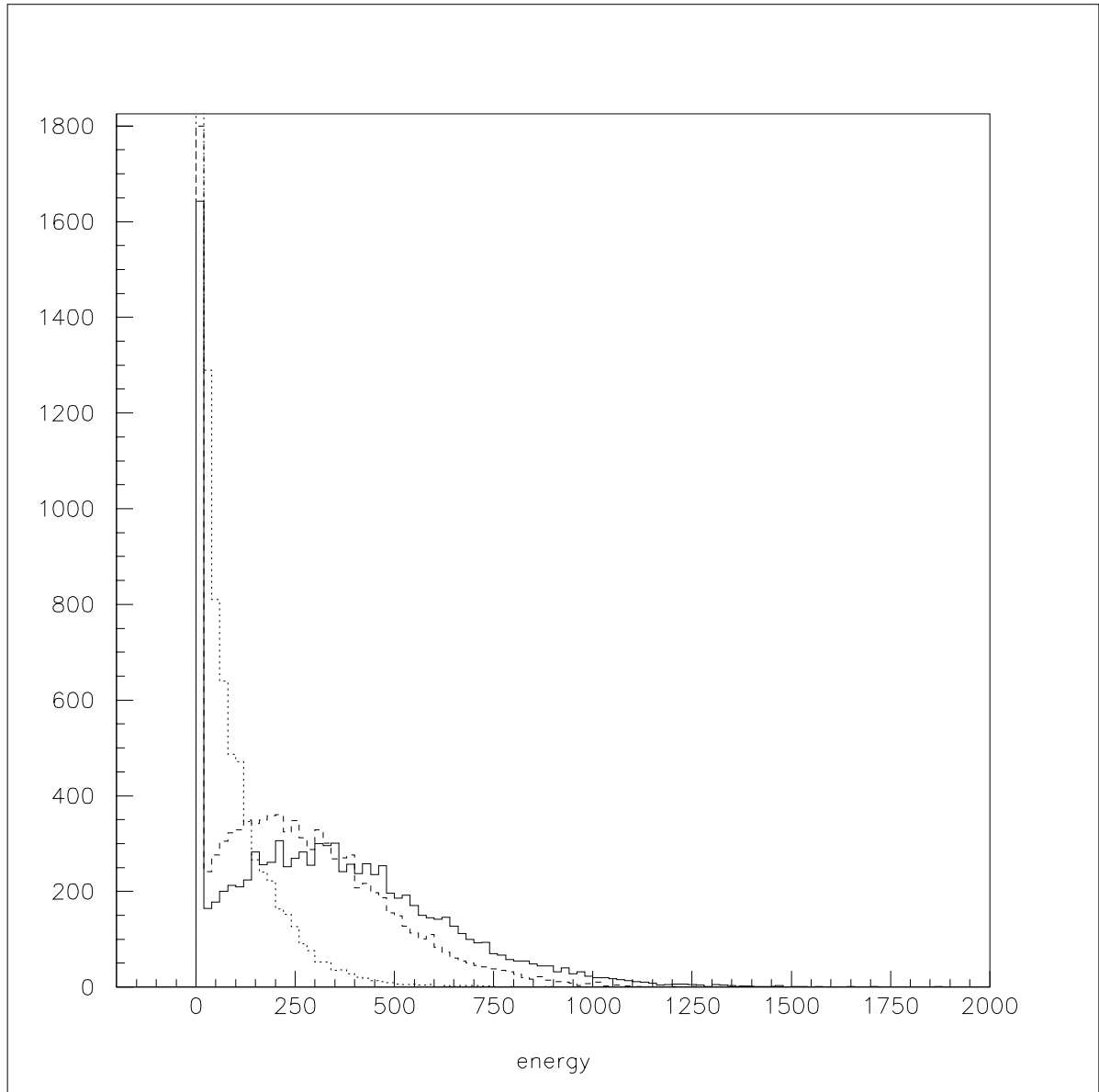


Figure 5.7: The energy outputs. The solid line represents the energy output of all 40 layers, the dotted line represents the energy output of the central 4 layers, and the dashed line shows the energy collected from the central 8 layers.

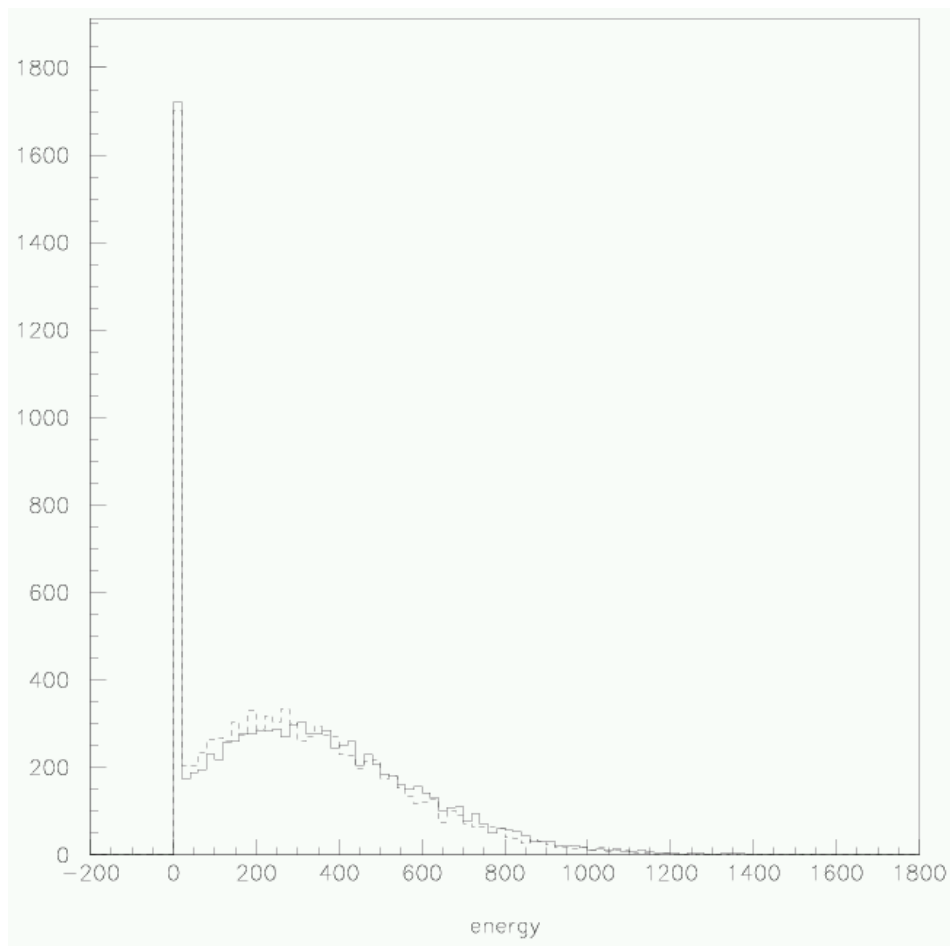


Figure 5.8: Comparison of energy outputs from simulations with neutrons sent into one spot (solid line) and spread around the face of the detector (dashed line).

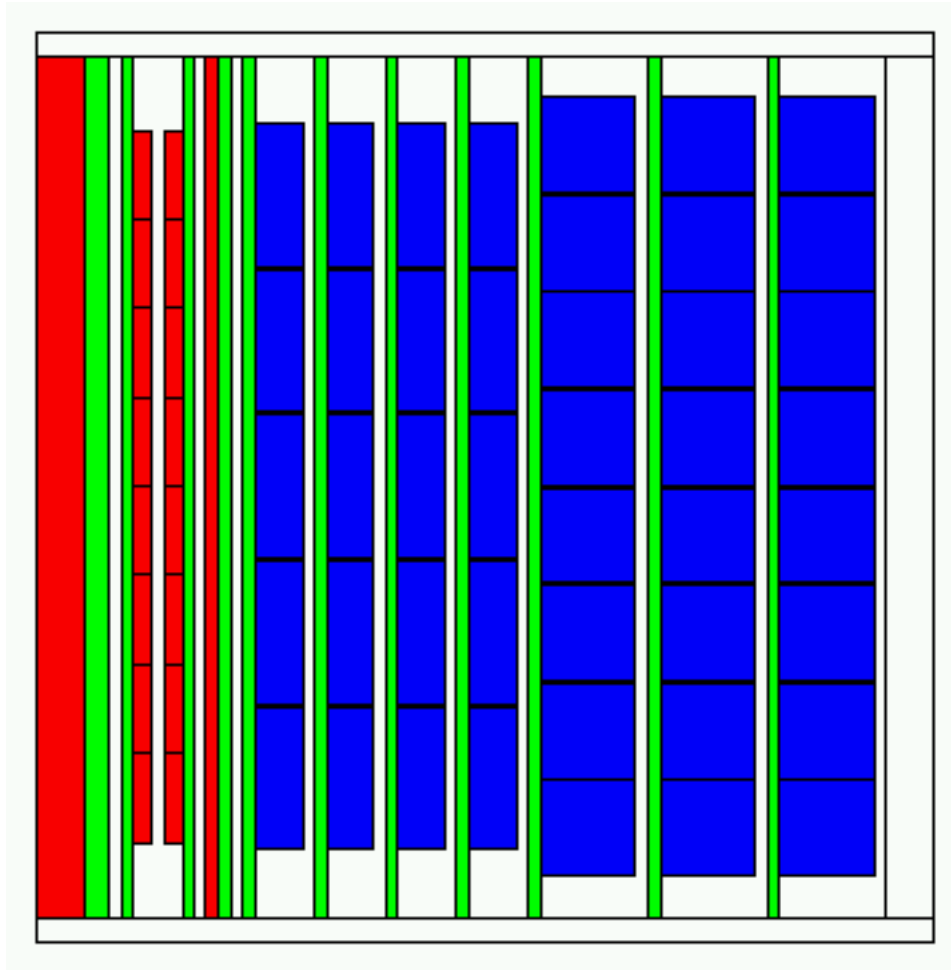


Figure 5.9: The neutron detector configuration for weighting coefficients analysis..

Chapter 6

Summary and conclusions.

We have performed a series of numerical simulations of the properties of the neutron detector for the JLab experiment E02-013, in which the electric form factor of the neutron G_E^N at high four-momentum transfer values of $Q^2 = 1.3, 2.4$ and $3.4 (GeV/c)^2$ in double polarized semi-exclusive quasi-elastic 3He scattering will be measured.

The numerical simulations tested the detection efficiency of different detector configurations, in particular, the influence of thicknesses of passive iron converters on the detection efficiency (see Table 5.1). As a result, we can conclude that the iron converters indeed improve the neutron detection efficiency with the thickness of 5.75 - 6.75 cm providing the best results (85-87%). For the future analysis, it was checked if giving different layers of detector bars different weights when analyzing the data helps to improve the signal to noise ratio in the data. Different functional forms were minimized and it was found that the simple noise to signal ratio provides good results. It was checked that different weighting coefficients give different background suppression and the best set of weighting coefficients was found (see Table 5.2).

The data from the test run, performed in 2003, was used to check how well the

simulations describe the actual data and the comparison showed a good agreement between those. This indicates the validity of using the aforementioned simulations for describing the actual experimental circumstances and predicting the data from the future experiment.

Appendix A

Theoretical models for nucleon form factors.

As long as experiments on determining form factors were going on, theoretical attempts of understanding the structure of nucleon were accompanying them. More than half a century of research brought forth a number of theoretical models describing them. Depending on the energy region the experimental data is in agreement with different models. In this section I'll survey some of the more important models.

A.1 Dipole parameterization.

The dipole approximation is the lowest order attempt to incorporate the non-pointlike structure of the proton into the form factors. It is a phenomenological parameterization. Early experiments [52, 53] found the following dipole approximation of the nuclear form factors to fit the proton data well:

$$G_E^p = (1 + Q^2 r_0^2)^{-2} = \frac{G_M^p}{\mu_p} = \frac{G_M^N}{\mu_n}, \quad (\text{A.1})$$

$$G_E^N = -\tau G_M^N, \quad (\text{A.2})$$

$$\tau = \frac{Q^2}{4M_n^2}. \quad (\text{A.3})$$

The nucleon form factors are related to the Fourier transform of the nucleon charge and this dipole form factor yields an exponential charge distribution for the proton:

$$\rho = \rho_0 \exp \frac{-r}{r_0}, \quad (\text{A.4})$$

where r_0 ($r_0^2 = 1.41(\text{GeV}/c)^{-2}$) is the scale of the proton radius and $\rho_0 = \frac{1}{8\pi r_0^2}$ is a normalization constant.

This model works well for low Q^2 , but it doesn't provide any real understanding of the underlying physics. Thus, the search for more physically motivated models proceeded.

A.2 Vector meson dominance models.

Vector meson dominance (VMD) models [54, 55] describe the photon-nucleon interaction via intermediate coupling with vector mesons, as shown in Figure A.1.

The form factor for the γ - N coupling through vector mesons can be written as:

$$F(Q^2) = \sum_i \frac{C_\gamma v_i}{Q^2 + M_{v_i}^2} F_{v_i N}(Q^2), \quad (\text{A.5})$$

where $\frac{1}{Q^2 + M_{v_i}^2}$ is the propagator associated with meson of mass M_{v_i} , $C_\gamma v_i$ is the photon-meson coupling strength and $F_{v_i N}(Q^2)$ is the meson-nucleon form factor.

In the VMD models the Dirac and Pauli form factors of the nucleon are written as a linear combination of the isovector and isoscalar form factors:

$$\begin{aligned} F_1^p &= F_1^{IS} + F_1^{IV}, & F_2^p &= F_2^{IS} + F_2^{IV}, \\ F_1^n &= F_1^{IS} - F_1^{IV}, & F_2^n &= F_2^{IS} - F_2^{IV}. \end{aligned} \quad (\text{A.6})$$

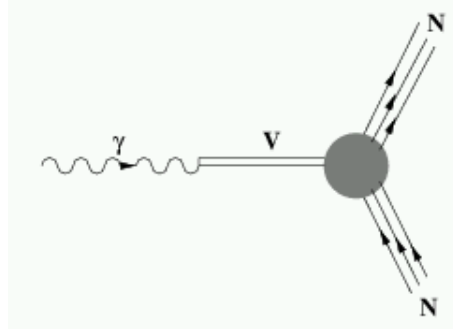


Figure A.1: The photon-nucleon coupling in the vector meson dominance model.

The neutron consists of an infinite series of pointlike partons and mesons arising from the vacuum for a brief moment and coupling to each other. The virtual photon fluctuates into a hadron with the same quantum numbers (charge, strangeness, spin) to form the vector mesons (ρ , ω) enhancing the strength of interactions. There are different VMD models depending on the inclusion of different meson states.

A.3 Gari-Krümpelmann model.

The Gari-Krümpelmann's (G-K) model [56] combines the low Q^2 phenomenology of VMD with the high Q^2 prediction of perturbative QCD. This model incorporates in a simple way the constraints from meson dynamics at low Q^2 and the asymptotic predictions from p-QCD at high Q^2 . Both the Dirac and Pauli form factors follow a monopole type Q^2 dependence at low Q^2 where meson physics dominates. At high Q^2 they follow p-QCD asymptotic behavior: $F_1^p \sim 1/Q^4$ and $F_2^p \sim 1/Q^6$. Within the

G-K model, the isovector and isoscalar form factors were parameterized by:

$$\begin{aligned}
F_1^{IV} &= \left\{ \frac{M_\rho^2}{M_\rho^2 + Q^2} \frac{g_\rho}{f_\rho} + 1 - \frac{g_\rho}{f_\rho} \right\} F_1^{QCD}, \\
F_1^{IS} &= \left\{ \frac{M_\omega^2}{M_\omega^2 + Q^2} \frac{g_\omega}{f_\omega} + 1 - \frac{g_\omega}{f_\omega} \right\} F_1^{QCD}, \\
k_v F_2^{IV} &= \left\{ \frac{M_\rho^2}{M_\rho^2 + Q^2} \frac{g_\rho}{f_\rho} k_\rho + k_v - \frac{g_\rho}{f_\rho k_\rho} \right\} F_2^{QCD}, \\
k_s F_2^{IS} &= \left\{ \frac{M_\omega^2}{M_\omega^2 + Q^2} \frac{g_\omega}{f_\omega} k_\omega + k_s - \frac{g_\omega}{f_\omega k_\omega} \right\} F_2^{QCD}, \\
F_1^{QCD} &= \frac{\Lambda_1^2}{\Lambda_1^2 + \hat{Q}^2} \frac{\Lambda_2^2}{\Lambda_2^2 + \hat{Q}^2}, \quad F_2^{QCD} = \frac{\Lambda_2^2}{\Lambda_2^2 + \hat{Q}^2} F_1^{QCD}, \\
\hat{Q}^2 &= Q^2 \ln \left\{ \frac{\Lambda_2^2 + Q^2}{\Lambda_{QCD}^2} \right\} / \ln \left\{ \frac{\Lambda_2^2}{\Lambda_{QCD}^2} \right\},
\end{aligned} \tag{A.7}$$

where $k_v = k_p - k_n$ and $k_s = k_p + k_n$ and k_p and k_n are the anomalous contributions to the proton and neutron magnetic moments respectively. Λ_1 is the scale of the proton wave function ($\sim 0.8 GeV$) and Λ_2 is the scale separating the meson physics dominance from the quark dynamics dominance.

The model was fit to proton and neutron form factors from measured electron scattering cross-sections using $M_\rho = 0.776 GeV/c^2$ and $M_\omega = 0.784 GeV/c^2$. The best fit parameters were:

$$\begin{aligned}
\Lambda_1 &= 0.795 GeV, \quad \Lambda_2 = 2.27 GeV, \quad \Lambda_{QCD} = 0.29 GeV \\
\frac{g_\rho}{f_\rho} &= 0.377, \quad k_\rho = 6.62, \quad \frac{g_\omega}{f_\omega} = 0.411, \quad k_\omega = 0.163.
\end{aligned} \tag{A.8}$$

The p-QCD effects begin to dominate the form factor at $Q^2 = \Lambda_2^2 = 5.15 (GeV/c)^2$.

The G-K model has been extended by including ϕ -meson exchange in the isoscalar form factors [57]. This inclusion significantly affects the neutron charge form factor. The Saclay data on G_E^N [58] extracted using the Paris potential favor the inclusion of the ϕ -meson exchange, while recent high precision results on proton form factors [7, 59] prefer the model that excludes it.

A.4 Quark models.

In the quark model hadrons are represented as bound states of two and three quarks.

Flavor	I	I_3	S	C	B^*	T	Q/e
u	1/2	1/2	0	0	0	0	2/3
d	1/2	-1/2	0	0	0	0	-1/3
s	0	0	-1	0	0	0	-1/3
c	0	0	0	1	0	0	2/3
b	0	0	0	0	-1	0	-1/3
t	0	0	0	0	0	1	2/3

Table A.1: Quark quantum numbers. I, I_3 , B, S, C, B^* , T, $Q/e = I_3 + \frac{1}{2}(B + S + C + T + B^*)$ denote the isospin, the third component of isospin, the baryon, strangeness, charm, beauty, top quantum numbers and electric charge respectively.

The quantum numbers of quarks are listed in Table A.1. The quarks have an additional quantum number or property - color (red, blue, green) and are confined by strong color forces through gluons inside the hadrons. The strong interaction coupling constant is asymptotically free, that is, $\alpha_s(Q^2)$ approaches zero at short distances and perturbation theory can be used there.

Many quark models exist. They differ in the way they mock up the effects of confinement and in the symmetries the quark wave functions have. The models include bag models, quark models with hyperfine interactions, constituent quark models and diquark models.

A.4.1 Bag models.

Within the MIT Bag model [60, 61], the baryon system consists of three noninteracting massless quarks, which are confined in a bag of radius r , essentially an infinite square well confinement potential. The bag radius is a free parameter. The one-gluon exchange interaction is treated as a perturbation. The MIT bag model is not chiral

invariant. The axial current (J_5) associated with the MIT bag model does not respect chiral symmetry even in the limit where quark masses are zero (“chiral limit”).

To restore chiral invariance (in the limit $m_\pi \rightarrow 0$), the cloudy bag model (CBM) was developed [62]. In CBM the bag is surrounded by a cloud of pions moving freely everywhere except for the bag surface where they can be absorbed or emitted. The absorption and emission obey chiral symmetry. Within the CBM the virtual photon couples either directly to the quarks inside the bag or interacts with the pion field. The neutron mean square charge radius $\langle (r_E^n)^2 \rangle$ obtained from this model ranges from -0.107 fm^2 to -0.153 fm^2 as the bag radius varied from 1.1 fm to 0.7 fm, which is in good agreement with the recent experimental value of -0.113 fm^2 . By eliminating the center of mass motion via several different momentum projection techniques and appropriately taking the Lorentz contraction of the internal structure of the baryon into account, it is found that the nucleon form factors agree with experimental data for a bag radius of around 1.0 fm, a larger bag radius corresponding to a smaller value of G_E^N .

The neutron electric form factor is very small, as the charge of the valence quarks adds up to zero. Therefore G_E^N is expected to be very sensitive to sea quark contributions in the nucleon. This is demonstrated in the model of Gorsky *et al.* [63] based on the Nambu-Jona-Lasinio (NJL) Lagrangian. The quarks are not confined in a bag but the Lagrangian is built such that the quarks are effectively confined. It is a simple quark model which includes spontaneous breaking of chiral symmetry and it predicts that the valence quarks and the sea quarks contribute to G_E^N with similar magnitude and opposite sign. At large radii ($r > 1.0 \text{ fm}$) the charge distribution of the neutron is dominated by the sea quark distribution.

A.4.2 Quark model with hyperfine interactions.

The neutron electric form factor has been calculated by Isgur, Karl and Sprung [64] in a model based on the color hyperfine interactions which add mixed symmetry components into the nucleon spatial wave function. In their model the unperturbed ground state (${}^2S_{S\frac{1}{2}+}$) is mixed with the nearby nucleon excited states (${}^2S'_{S\frac{1}{2}+}$, ${}^2S_{M\frac{1}{2}+}$ and ${}^4D_{M\frac{1}{2}+}$). The resultant SU(6) violations are then a good test for hyperfine interactions.

While the admixture of the ${}^4D_{M\frac{1}{2}+}$ state in the nucleon is predicted to be small and the admixture of the radial excitations, ${}^2S'_{S\frac{1}{2}+}$, is difficult to detect, the admixture of the ${}^2S_{M\frac{1}{2}+}$ states gives rise to the observed charge radius of the neutron. The non-zero neutron charge distribution of the neutron can be viewed as follows: the two identical d quarks in the 2S_S neutron must have S=1 to satisfy the Pauli exclusion principle. They repel each other due to their parallel spins; on the other hand, the two u - d quark pairs attract each other; this results in a distorted neutron wave function which breaks the SU(6) asymmetry. As a result, this pushes the d quarks to the periphery of the neutron and pulls the u quark into the center, thus creating a charge segregation inside the neutron and leading to a non-zero G_E^N .

The model predicts the neutron and proton charge form factors to the leading non-vanishing order in the mixing coefficients (i.e. to order α_s) using the harmonic oscillator model and finds:

$$G_E^N(Q^2) = -\frac{1}{6} \langle (r_E^n)^2 \rangle Q^2 e^{-Q^2/6\alpha_s^2}, \quad G_E^p(Q^2) = e^{-Q^2/6\alpha_s^2}. \quad (\text{A.9})$$

The model predicts that the maximum of G_E^N occurs at $Q^2 \simeq 0.36(\text{GeV}/c)^2$. The resulting G_E^N agrees with the data from Galster *et al* [12] very well.

A.4.3 Constituent quark models.

The nonrelativistic approximation of the quark models is problematic since the effective quark masses and the intrinsic momenta have the same order of magnitude. Attempts to implement relativistic invariance for the description of the electromagnetic properties of nucleon constitute the covariant constituent quark models by Koken and Weber [65] and Chung and Coester [66], which use light front dynamics for the constituent quarks.

In the relativistic constituent quark model, the constituent quarks are extended objects with masses of ~ 300 MeV and hence have form factors associated with them. In this model there are two free parameters; the quark confinement scale $1/\alpha_s$, and the quark mass m_q .

In this framework, the available experimental data for $0 \leq Q^2 \leq 1.5(\text{GeV}/c)^2$ [65] and $0 \leq Q^2 \leq 6.0(\text{GeV}/c)^2$ [66] have been well described with two adjustable parameters.

Recently, the nucleon form factors within a relativistic three-quark model with a Gaussian shape for the nucleon-quark vertex and standard (not confined) quark propagators were calculated [67]. Gauge invariance of the hadron-quark interaction has been implemented by a path independent definition for the derivative of the time-ordering P-exponent. The two adjustable parameters, the range parameter Λ_N and the constituent quark mass m_q , have been obtained by fitting the data for the magnetic moments and electromagnetic radii of the nucleons. Even with reasonable values of $\Lambda_N = 1.25$ GeV and $m_q = 420$ MeV, the model underestimates the proton electromagnetic form factors and the neutron magnetic form factor, but overestimates the neutron electric form factor at high Q^2 in the calculated range of $0 \leq Q^2 \leq 1(\text{GeV}/c)^2$.

A.4.4 Diquark model.

At high Q^2 , even with a relativistic invariant framework, the constituent quark model is unable to describe the measured form factors. This shortcoming is due to the exponential fall-off with respect to Q^2 of the single particle wave function in the confining potential.

In this model, the three-body physics of the nucleon was simplified by introducing two tightly bound quarks called a "diquark" ($r \sim 0.1-0.3$ fm) and a single constituent quark. The diquark is treated as a quasi-elementary particle. Q^2 dependent form factors were introduced to account for the finite size of the diquark. The resulting two-body system was treated perturbatively. The quarks comprising the diquark provide spin 1 and 0 coupling which allows for helicity flips. The model of Kroll *et al.* [68] describes the experimental data for nucleon form factors at intermediate Q^2 well.

A.5 Theoretical predictions on G_E^N .

Figure A.2 shows the predictions of the Q^2 dependance of G_E^N in the different theoretical models discussed in this appendix and the Galster parameterization fit.

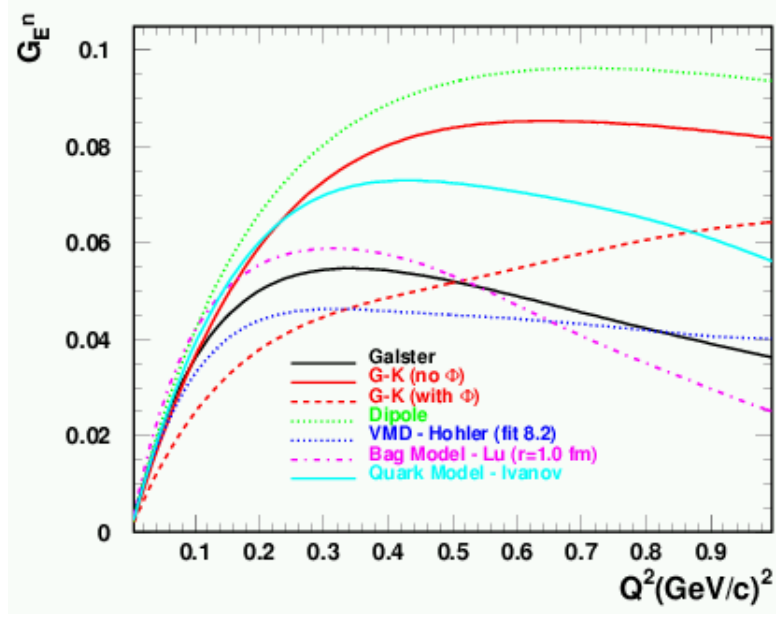


Figure A.2: $G_E^N(Q^2)$ in various theoretical predictions compared to the Galster parameterization.

Appendix B

Helicity asymmetry in ${}^3\vec{He}(\vec{e}, e'n)$ and the ratio of G_E^N/G_M^N .

B.1 Nucleons in the nuclear medium.

There are several processes related to the influence of the nuclear medium on the structure of the bound nucleon. One of the best known is the nuclear EMC effect, which shows that the structure function of the nucleus is suppressed at large x_{B_j} relative to that of the deuteron. While a definitive explanation of this effect is still elusive, it is clear that a quantitative description of the effect requires, in addition to the conventional nucleon and meson degrees of freedom, some dynamical effects involving sub-nucleonic degrees of freedom (*e.g.*[69, 70]). However two factors make the EMC controllable in the measurement under discussion. First of all, in models where the EMC effect is proportional to the virtuality of the bound nucleon, which would potentially lead to a distortion of the intrinsic structure of the bound nucleon, the restriction to small values of missing momenta will substantially suppress any such

distortion and the corresponding onset of the EMC effect. Secondly, the measured asymmetry will be less sensitive to nucleon structure modifications since the bulk of the EMC effect will be less revealed in the form factor ratios.

Color transparency (CT) is the next effect (*e.g.*[70]) that can potentially hinder the extraction of the neutron form factor at high Q^2 . This effect has been investigated in quasi-elastic proton knock out by electrons for nuclei for Q^2 from 1 to 8 $(GeV/c)^2$ [47]. Such studies probe the propagation of the nucleon through nuclei and test the effect of the nuclear medium on the proton knockout cross-section. The aforementioned experiment [47] observed no signature for CT up to $Q^2 = 8(GeV/c)^2$ in the kinematics of restricted missing momentum and energy. Moreover, the comparison with theoretical calculations demonstrated that the Glauber approximation adequately describes the data for a wide range of nuclei (ranging from deuteron to iron). Thus for the Q^2 of this experiment one expects that the Glauber approximation will reliably describe the final state interactions in the 3He reaction.

A study of polarization observables in the reaction ${}^4He(\vec{e}, e'\vec{p})$ was made recently [71]. This experiment found that the ratio of the components of the polarization of the recoiling proton P'_x/P'_z is smaller than the same ratio of the hydrogen target by about 10% (see Fig.B.1). The same effects that contributed to this modification need to be taken into account for the analysis of ${}^3\vec{He}(\vec{e}, e'n)$. The lower density of a 3He nuclei compared to a 4He nuclei will lead to a proportional reduction of these medium effects. Calculations from J.Udias predict a reduction of the ratio P'_x/P'_z of 8% in 4He compared to hydrogen, whereas in 3He the reduction is only 4% .

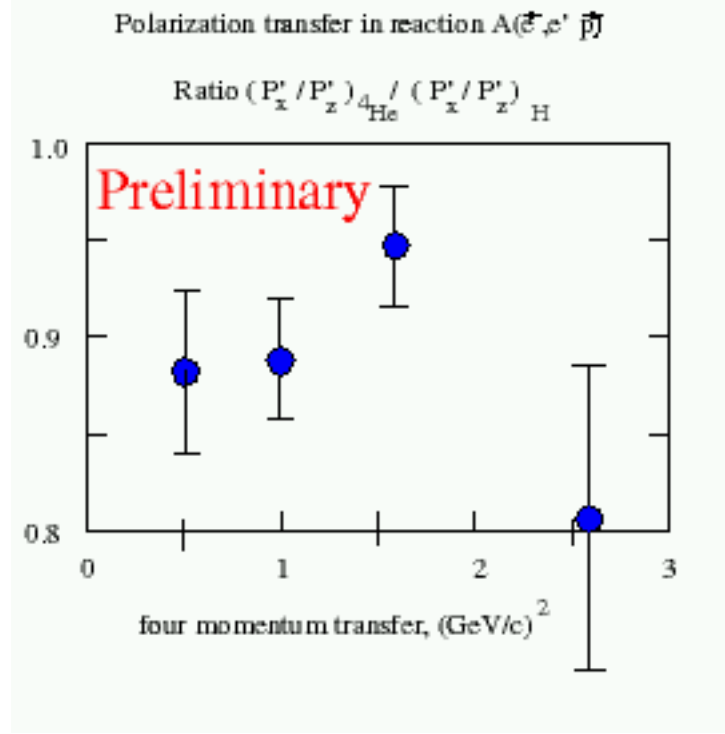


Figure B.1: The ratio of the polarization transfer components for a bound proton relative to the free proton.

B.2 ${}^3\vec{H}e$ as a neutron target.

Experiments utilizing ${}^3\vec{H}e$ targets as effective neutron targets have been carried out for a wide range of beam energies at Bates, Indiana, NIKHEF, Mainz, HERMES, SLAC, and JLab. During the past decades there have been several theoretical discussions about the possibility of using a ${}^3\vec{H}e$ target to study properties of the elastic electromagnetic form factors of the neutron [16, 33, 72]. In addition, calculations for inclusive and exclusive electron scattering reactions from ${}^3\vec{H}e$ have been performed [72, 73].

The neutron polarization in ${}^3\vec{H}e$ and the three-nucleon wave function have been

computed by a number of authors using several different methods, including the approach via Faddeev equations [74], and the variational approach [27, 29, 30, 31, 32].

The semi-exclusive reaction ${}^3\vec{H}e(\vec{e}, e'n)$ allows one to fix the values of the missing momenta and energy of the struck neutron which are the key parameters for controlling the size of nuclear effects. A cut on the transverse components of the neutron momentum p_{mperp} is more effective in this task than a cut on the longitudinal component p_{mpar} [75]. In the experiment the value of the asymmetry will be measured as a function of p_{mperp} in the range 0-150 MeV/c. This will allow for a check of the universality of the result and to extrapolate to low p_m^2 .

B.3 Qualitative assessments of nuclear effects in the extraction of G_E^N/G_M^N from semi-exclusive $A(e, e'N)X$ reactions.

The key observation driving the measurement of this experiment is that it's possible to select small momenta in the 3He wave function by requiring $p_{mperp} < 30$ MeV/c. This is the case because the good convergence of the integral $\Psi(k)dk$ (normalized as $\int \Psi^2(k)d^3k = 1$) leads to the selection of very small momenta in the wave function of 3He , even though the cut on p_{mpar} is not big (250 to 500 MeV/c). In our kinematics the effective cut on missing energy E_m is almost the same as the cut on p_{mpar} .

Additionally, these cuts ensure the suppression of the proton polarization, which is already a small factor ($< 3\%$), and suppress small non-nucleonic admixtures in the wave function. Furthermore, they significantly suppress the final state interactions, since the struck nucleon is rather far away from other nucleons. Besides, most of the

rescattering in this kinematics actually removes nucleons to larger transverse missing momenta p_t , and hence they do not affect asymmetries calculated in the PWIA in order to extract $R = G_E^N/G_M^N$.

The following is the assessment of nuclear effects that may affect this extraction, and some qualitative estimations indicating which corrections will possible to estimate more quantitatively.

1. Finite acceptance effects. Because the experiment will measure G_E^N within a finite interval of missing momenta p_m and missing energy E_m , the integration will smear out the extracted R. This effect is expected to be small if a tight cut on the p_{mperp} and a modest cut on E_m are applied.
2. Off-shell effects. The uncertainty associated with off-shell effects can be estimated by applying different off-shell prescriptions for calculation of nucleon currents. However, since the momenta of the struck nucleons are small, these effects, which are proportional to p_m^2/m_n^2 , should be strongly suppressed.
3. Meson exchange effects. The choice of high Q^2 causes a significant suppression of meson exchange effects in the extraction of R. At $Q^2 > 1(\text{GeV}/c)^2$ the overall additional Q^2 dependence of the MEC amplitude as compared to the plane wave impulse approximation amplitude will be $(1 + Q^2/\Lambda^2)^{-2}$, where $\Lambda^2 = 0.8 - 1 (\text{GeV}/c)^2$ [75]. Additionally, the MEC contribution will be suppressed due to the restriction of small p_{mperp} and E_m (usually MEC effects start to contribute at rather large nucleon momenta, of the order of 300 MeV/c). One way to estimate these effects is to take the theoretical calculations at small Q^2 and scale them according to the relation given above.

The proposed experiment will take data at $Q^2 = 1.31 (\text{GeV}/c)^2$, where the

measurements from [26, 25] were performed utilizing a deuteron target, so the experimental evaluation of nuclear effects can be performed.

4. Delta isobar contribution. This effect should be small because of the restrictions on p_m and E_m . If one assumes the same Q^2 and energy dependence of the elastic electromagnetic form factor as of the $N\Delta \rightarrow NN$ rescattering amplitude, one is able to estimate the Δ contribution using the FSI amplitude, but taking into account the fact that it corresponds to the larger p_{mpar} in the argument of the nuclear wave function. This gives the upper limit of the Δ contribution.

Preexisting Δ -isobars in 3He have a rather small probability - about 2% - and they also have substantially larger average transverse momenta than nucleons. Hence the cut on small average nucleon momenta will lead to further suppression. Still this is a potential background since there can be a transition $\gamma^*\Delta^0 \rightarrow n$. One should remember that the Δ^0 is polarized. From the Bjorken sum rule one can expect the Δ contribution integrated over all momenta to be on the level of 4% times the ratio of the ΔN form factor and the NN form factor. An additional small factor mentioned above is the cut on momenta - so qualitatively one may get an effect on the scale of 1-2%.

5. Final state interactions (FSI). The major advantage is that at high Q^2 the eikonal approximation is applicable when the rescattering amplitude is practically energy-independent. First we discuss FSI due to diagonal elements of $np \rightarrow np$ rescattering matrix. In the case of the factorized approximation the uncertainty comes from the accuracy of the calculation of FSI contributions, which is less than 10%. The recent comparison of eikonal calculations with JLab data demonstrated a very good agreement for nuclear transparency start-

ing with deuteron and going up to iron [47].

In the case of small p_{mperp} and E_m , the overall effect of FSI for the ${}^3\text{He}$ target is 10-15%, thus the uncertainty due to the accuracy of FSI is 1-1.5%. The theoretical calculations will all allow an estimation of the uncertainty due to factorization.

Non-diagonal FSI is due to charge exchange rescattering.

In the high energy limit the charge exchange amplitude ($pn \rightarrow np$) is mainly real. The imaginary part at $Q^2 = 1-1.5 \text{ (GeV/c)}^2$ is 10-20% of the diagonal amplitude, thus one expects that charge exchange will contribute 1-2% in the overall FSI. The real part will contribute in the non-eikonal part of the rescattering as well as in the double rescattering. There is an additional small factor in the asymmetry amplitude since the proton is polarized very weakly in the kinematics chosen for the measurements. Since charge exchange goes through the pion exchange its amplitude decreases with s (compare the s -independence of diagonal $N N \rightarrow N N$ amplitude). The theoretical calculations will allow an estimate of this contribution.

To summarize, it appears that corrections to the impulse approximation will be significantly less than 10% (expected to be on the level of 2-5%), and most of these effects will be possible to correct for. The code will also provide the extraction algorithm which will allow extraction of R taking into account FSI terms.

B.4 Preliminary results of the GEA calculation.

GEA [75], a code based on the generalized eikonal approximation, was used for the calculations of A_{perp} shown in Fig.B.2. The asymmetries were calculated for a beam

energy of 3.244 GeV and assuming that G_E^N follows the Galster parameterization. The following cuts on the components of missing momenta were applied: p_{mperp} less than 50 MeV/c and p_{mpar} less than 250 MeV/c. The invariant mass cut was $W = 0.94 \pm 0.05$ GeV. The upper solid line represents the results of the code for a free neutron at rest. The lower solid line with smaller values of A_{perp} is a naive estimate of the asymmetry based on the neutron carrying 82% of the polarization of ${}^3\vec{He}$. The dash line presents the results of the PWIA calculation. The dotted line is the result of the distorted wave impulse approximation (DWIA) calculation. The dash-dotted line is the DWIA calculation with charge exchange (CE) effects included. The effect of CE is about 5.5% at $Q^2 = 4 (GeV/c)^2$, in agreement with the expectations.

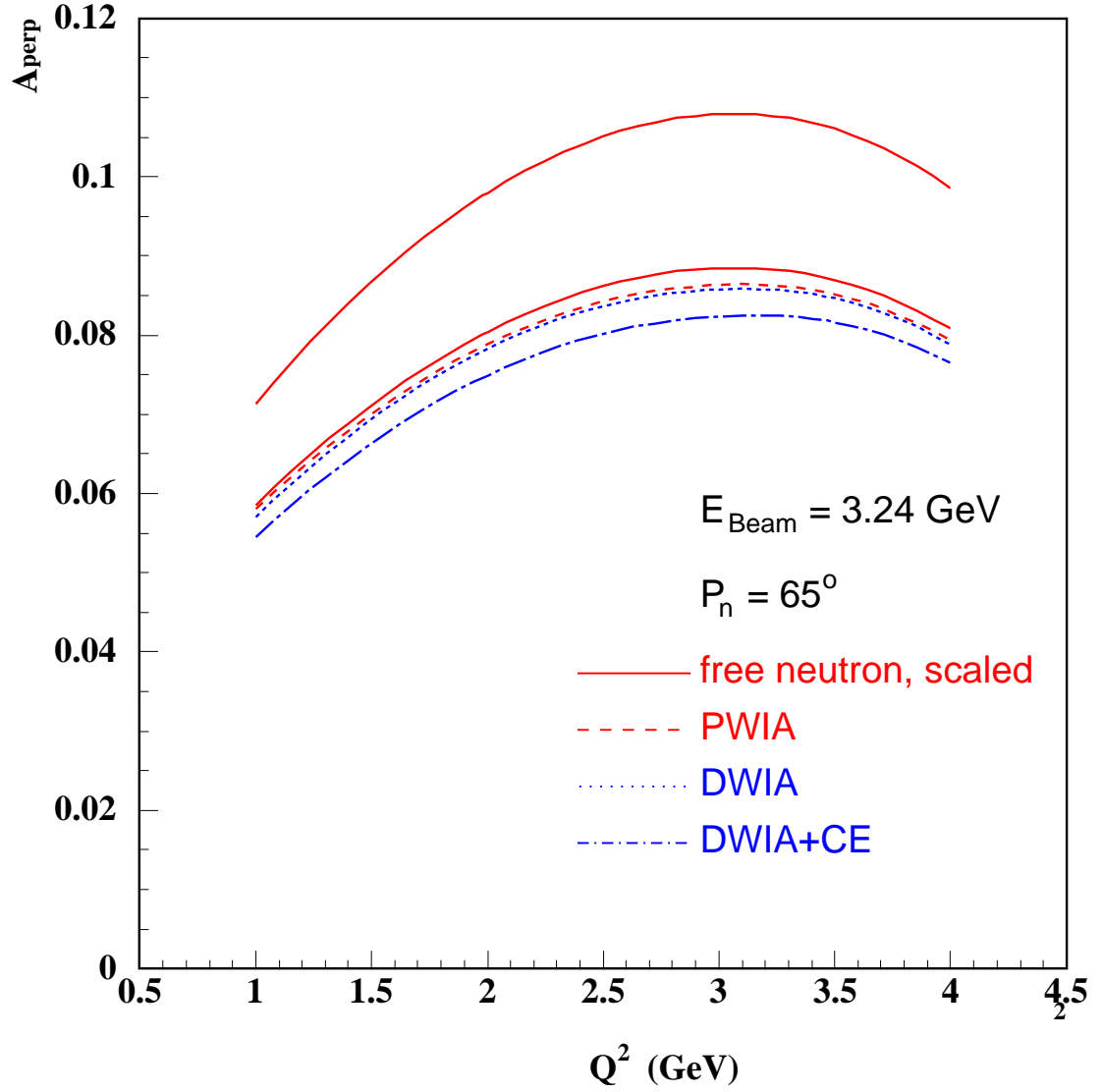


Figure B.2: The A_{perp} asymmetry calculated by Sargsian in the generalized eikonal approximation. The upper solid line represents a free neutron at rest. The lower solid line with smaller value of A_{perp} is a naive estimate of the asymmetry based on the neutron carrying 82% of the polarization of ${}^3\vec{He}$. The dash line represents the results of the PWIA calculation. The dotted line is the results of the DWIA calculation. The dash-dotted line is the DWIA calculation with CE effects included.

Appendix C

Quasi-elastic scattering at Q^2 of several $(GeV/c)^2$.

In this chapter I will discuss the physics and room background contributions to the data and the method of separating the quasi-elastic scattering (QES) events from the background. Several physics processes contribute to the background which the detectors will see, including inelastic scattering associated with pion production, single pion photo-production and quasi-elastic scattering from protons in ${}^3\vec{He}$. Inelastic scattering associated with pion production will be discussed in the first section. Single pion photo-production by virtual photons can be suppressed by using particle identification, as discussed in the second section. The suppression of quasi-elastic scattering from the protons in ${}^3\vec{He}$ requires a high efficiency of the veto detector in the neutron arm and will be discussed in the third section. The room background in the data comes from accidental coincidences due to the high rates of low energy neutrons and pions, which will be discussed in the fourth section.

C.1 Selection of QES events.

The first step in the extracting G_E^N is the selection of the quasi-elastic scattering events. We used experimental data from ${}^3\text{He}(e, e'p)$ reaction measured with Hall B CLAS detector at an incident beam energy of 4.4 GeV to study the effects of restrictions on missing momenta on the selection of QES events [38]. The resolutions achieved in this Hall B experiment are higher than what we will achieve in our setup. However in the following analysis all cuts are chosen in a way which can easily be realized for the analysis of the data from our measurement with the projected momentum and angular resolutions.

The upper part of Fig.C.1 shows the inclusive electron spectrum at $Q^2 = 3.5(\text{GeV}/c)^2$ which is close to the future measurements. The data are shown as a function of invariant mass $W = \sqrt{m_N^2 + 2m_N(E - E') - Q^2}$. In the inclusive spectra for $Q^2 = 3.5(\text{GeV}/c)^2$, the QES peak appears as a very small contribution to the spectrum intensity near $W=1$ GeV. However, if one looks at the coincidence data in Fig.C.3, the spectra are much cleaner. The figure displays the p_m distribution for five ranges of W . For $W = 0.95 \pm 0.1$ GeV the peak at low p_m dominates. In the range $p_m < 250$ MeV/c the level of non-QES contributions is below a few percent. These pictures show how the inelastic contribution grows with growing W .

The details of the spectra for $W = 0.95 \pm 0.1$ GeV at low values of p_m are shown in Fig.C.2, where the QES peak was fitted by the function $p_m^2 \exp(-p_m^2/(2p_a^2))$ and the non-QES part by the function $p_m^2/(1 + p_m^2/p_b^2)$.

Figure C.4 shows the event distribution versus the value of $p_{m\text{perp}}$, which is the part of the nucleon momenta perpendicular to the momentum transfer vector \vec{q} . In this figure, a loose cut on $p_{m\text{par}}$ was applied (≤ 0.5 GeV/c), which is the part of

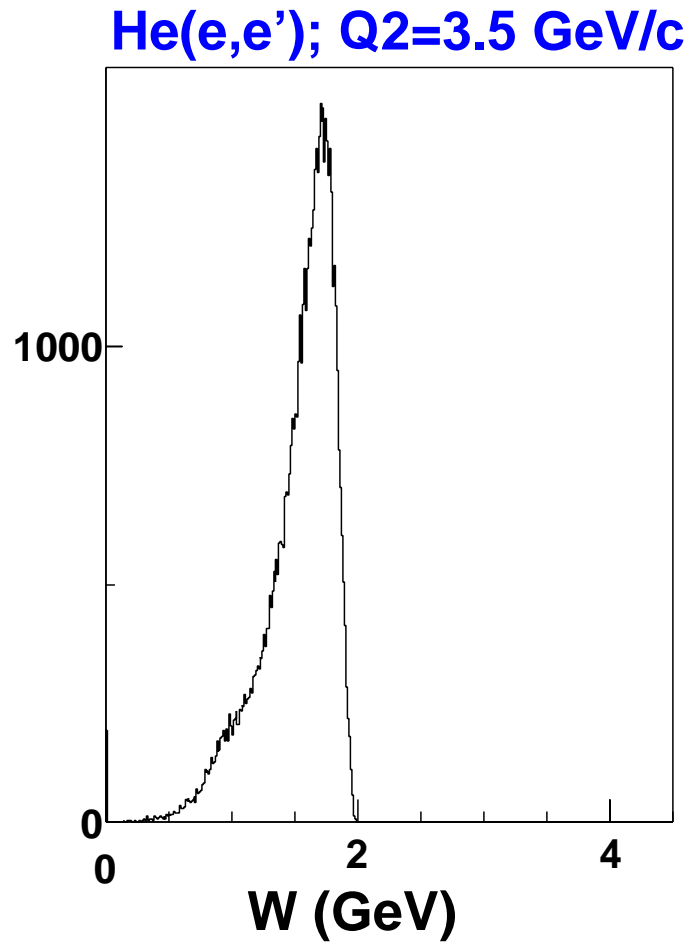


Figure C.1: The inclusive electron spectrum for the reaction ${}^3\vec{H}e(e,e')p$ at an incident energy of 4.4 GeV $Q^2 = 3.5 \text{ GeV}/c^2$ for the invariant mass distribution. The scale is in GeV.

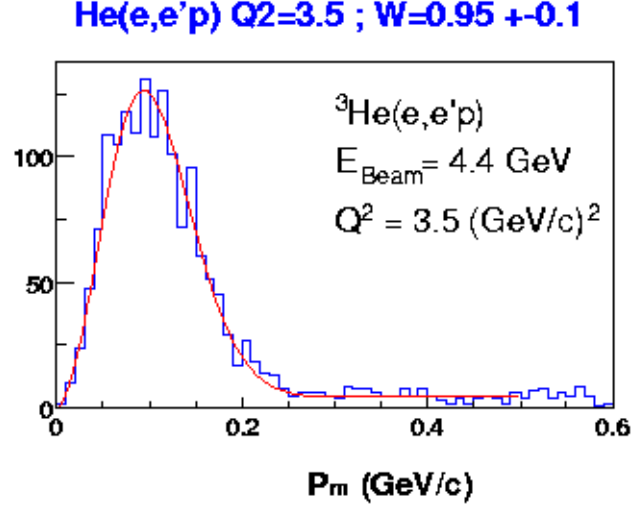


Figure C.2: A fit for the p_m distributions for $W = 0.95 \pm 0.1$ GeV/c. The scales are in GeV/c.

the nucleon momenta parallel to the momentum transfer vector \vec{q} . Here the peak was fitted by the function $p_{mperp}^2 \exp(-p_{mperp}^2/(2p_a^2))$ and the non-QES part by the function $p_{mperp}^2/(1 + p_{mperp}^2/p_b^2)$.

Our Monte-Carlo simulations show that the detector setup will provide a W resolution of 50 MeV, a p_{mperp} resolution of 250 MeV/c, and a p_{mperp} resolution of 30 MeV/c. These parameters will allow us to do a data analysis similar to the one described above for the CLAS data. The quality of the separation between QES and non-QES events will be the same as shown in Fig.C.4. In this case a clean extraction of QES events will be possible, and the background remaining from non-QES events will be less than 5%.

The analysis shown above is focused on the range of $W = 0.95 \pm 0.1$ GeV, which contains about 60% of all QES events. To get nearly all of the QES events, it is

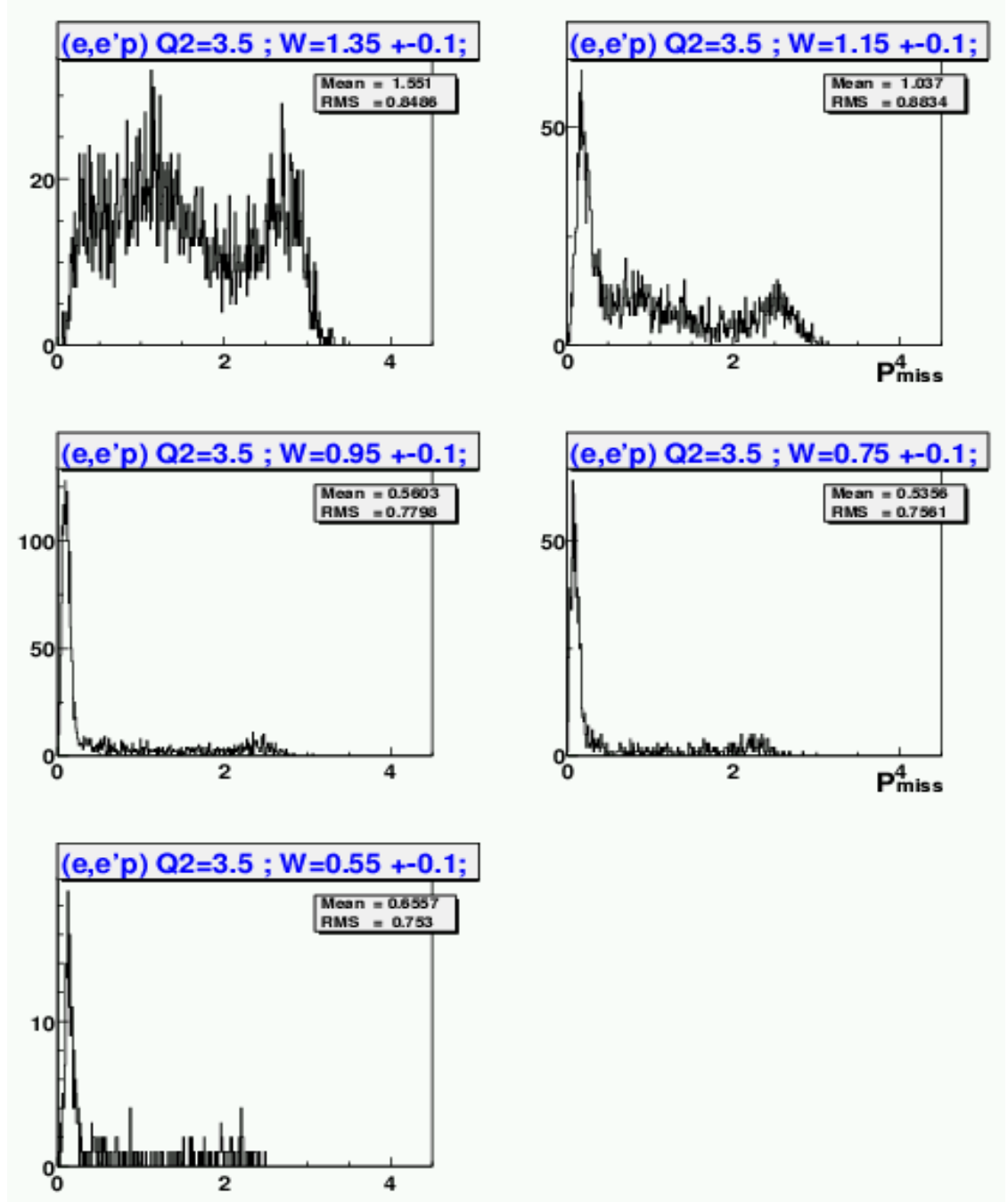


Figure C.3: The p_m distributions for ${}^3\vec{H}e$ ($e,e'p$) at Q^2 of 2.5 (GeV/c)^2 and 3.5 (GeV/c)^2 for five W values. The scales are in GeV/c .

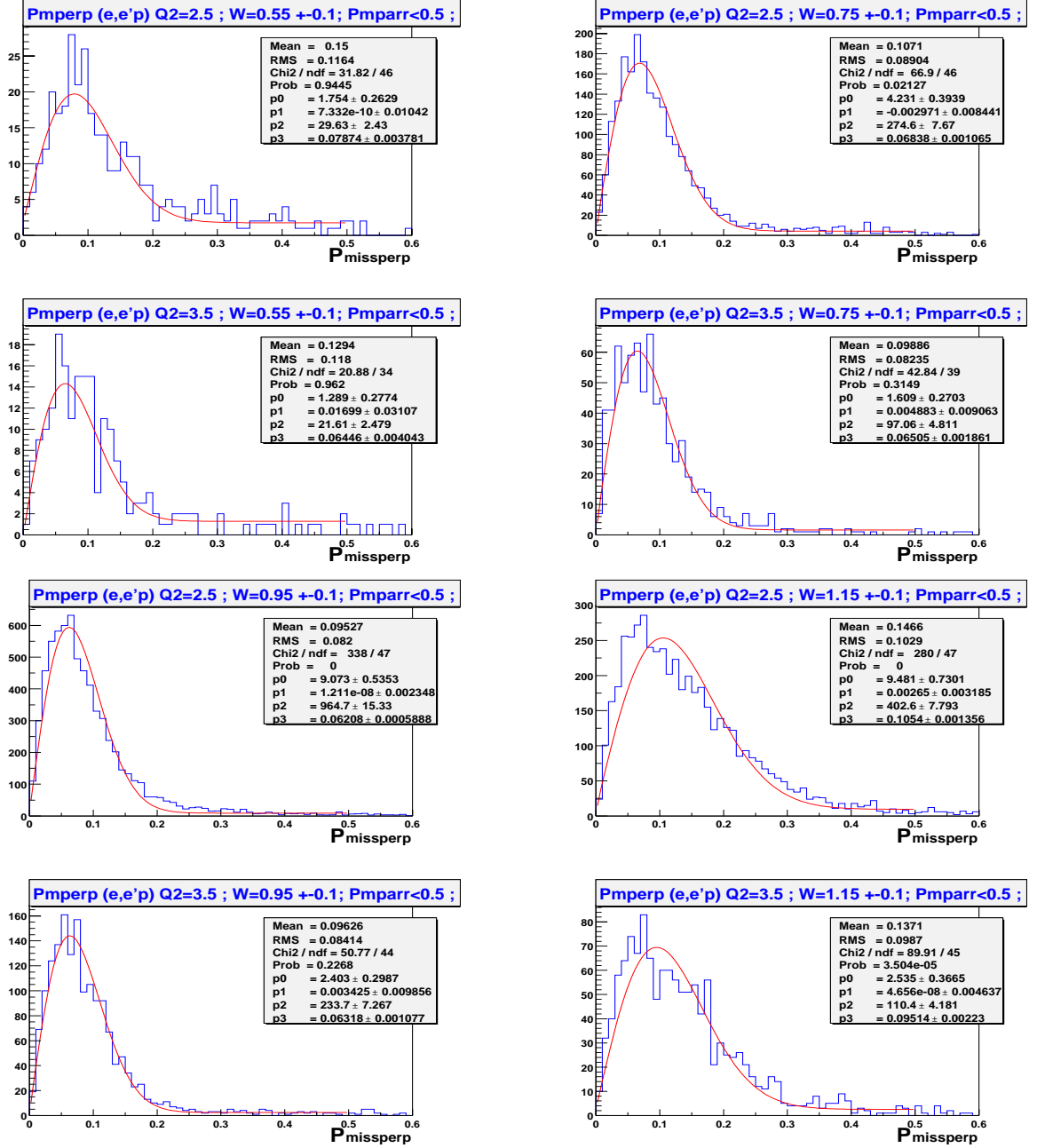


Figure C.4: The fit of p_{perp} distributions for four W ranges with the cut on p_{par} . The scales are in GeV/c.

necessary to analyze data for W up to 1.15 GeV. The scan of W from 0.45 to 1.25 GeV confirms that it is possible to use events with W from 0.45 up to 1.15 GeV after applying cuts on the missing momenta p_{mpar} (see Fig.C.4). The asymmetry in the background events will be analyzed in the large p_{mperp} region.

C.2 Photo-production of charged pions.

For estimating the photo-production rate of positive pions from the ${}^3\vec{H}e$ target we used the value of the cross-section from free protons and took the number of protons in 3He into account. In the photon energy range above 2 GeV and at large Θ_{CM} , the cross-section for the single pion production is $d\sigma / dt \approx 20mb/s$, where t is momentum transfer and s is $m_N^2 + 2m_N E_\gamma$ in $(GeV/c)^2$. In this reaction particles have almost the same kinematical correlations as in QES. The range of photon energies which need to be considered is defined by the acceptances of the two detectors. The angular correlation between the pion and neutron leads to a cutoff of coincidences at photon energies below 2.1 GeV (here we are considering the case at highest Q^2 point with an electron beam energy of 3.244 GeV). The intensity of real and virtual photons at $E_\gamma = 2$ GeV and higher was estimated to be 0.5% of the electron beam intensity times dE_γ/E_γ . The total rate of pion-neutron events was found to be of the order of 30 Hz. Pion rejection will be performed off-line by means of the lead glass shower counter (a factor of 100) and rejection based on the track analysis, because of the positive curvature of π^+ tracks (a factor of 50, limited by background hits in the MWDC). An additional reduction by a factor of 2 comes from the analysis of the correlation between the pion momenta and the lead glass signal. The resulting rate of 0.003 Hz corresponds to a 0.7% contamination of the sample of QES events.

Negative pion production from the neutron in ${}^3\vec{H}e$ leads to a two time smaller rate of events with a high energy proton in the neutron detector. Such events will be rejected by means of the veto detector on the proton side (factor of 30-50) and the lead glass counter on the pion side (factor of 100).

The background from the glass windows of the target cell and other windows will be cut out in the analysis by using cuts on the reconstructed coordinate along the target.

C.3 QES from the protons in ${}^3\vec{H}e$.

The rate of QES from the bound protons in 3He is about a factor of four-five higher than in the process under study. The use of plastic scintillator counters as a veto detector is a well developed technique. The veto detector can be segmented because of the good spatial resolution of the neutron bars, which enables the localization of the area where the check in the veto needs to be performed. The segmentation of the veto reduces the rate per detector and solves the problem of electronics (and PMT) dead time. Still, at the luminosity of this proposal the veto detector inefficiency is expected to be 1-1.5%. This parameter will be measured during the experiment by using the second layer of the veto which covers only a small portion of the neutron detector and is used mainly for the measurement of the veto efficiency. The remaining background will be on the level of 5%. The protons in ${}^3\vec{H}e$ have a low polarization so such background is much less important than in the case of G_E^N experiment using deuteron targets. Because the efficiency will be measured, the contribution of this background to the systematics in the asymmetry measurement is about 1-1.5%.

The nuclear interaction of the protons with the material between the target and

the veto detector was discussed in the neutron detector section. It will lead to an inefficiency of about 0.5%.

C.4 Accidental background.

The DAQ rate is expected to be on the level of 2.5 kHz with a coincidence time window of 25 ns. This rate corresponds to a 50 MeV threshold in the neutron arm and triggering of the electron arm from a two layer plastic scintillator trigger plane. The off-line analysis will use a 150 MeV threshold in the neutron arm and the lead glass shower detector for suppression of the pion events in BigBite. This analysis will bring the rate to 10 kHz in each arm. The 2.5 ns time window will reduce the rate of accidentals to 0.25 Hz. The fraction of background events in the range of p_{mperp} from 0 up to 150 MeV/c is 11%. The irreducible rate of 0.027 Hz corresponds to a 6% background for detected ${}^3\vec{H}e(\vec{e}, e'n)$ events. Because of several means to measure the amount of background of this type, its contribution to the systematics of the asymmetry measurement will be on the level of 1%.

C.5 Analysis of the raw asymmetry and extraction of A_{perp} .

The raw helicity asymmetry in the rate of QES electron-neutron events in a given range of Q^2 and p_{mperp} will be corrected for the degree of polarization of the ${}^3\vec{H}e$ nuclei in the target, for the beam polarization, for the dilution factor, and also for the background asymmetry. The result of this first analysis step is A_{phys} , which has contributions from both A_{long} and A_{perp} because of the large angular acceptance of

the electron arm. The systematics of the A_{long} calculation are expected to be on the level of 0.001 for an angular alignment accuracy of 1 mr. The averaged value of A_{long} is expected to be -0.007, which is about 15 times smaller than A_{perp} , which is expected to be about 0.108. A_{long} will be calculated based on the direction of target polarization and the acceptance of BigBite. The averaged A_{phys} corrected for the acceptance factor allows the extraction of A_{perp} with a systematic uncertainty smaller than 1%. The next step is to relate the value of A_{perp} to A_T for the free nucleon (see the previous chapter).

Bibliography

- [1] J.Chadwick, Proc. Roy. Soc. **A136**, 692 (1932).
- [2] R.Frisch and O.Stern, Z. Phys. **85**, 4 (1933).
- [3] E.Chambers and R.Hofstadter, Phys. Rev. **103**, 1454 (1956).
- [4] R.Walker *et al.*, Phys. Rev. **D49**, 5671 (1994).
- [5] L.Andivahis *et al.*, Phys. Rev. **D50**, 5491 (1994).
- [6] A.Sill *et al.*, Phys. Rev. **D48**, 29 (1993).
- [7] M.Jones *et al.*, Phys. Rev. Lett. **84**, 1398 (2000).
- [8] O.Gayou *et al.*, arXiv:nucl-ex/0111010, submitted to Phys. Rev. Lett. Nov.15, 2001.
- [9] H.Anklin *et al.*, Phys. Lett. **B428**, 248 (1998).
- [10] E.Bruins *et al.*, Phys. Rev. Lett. **75**, 21 (1995).
- [11] A.Lung *et al.*, Phys. Rev. Lett. **70**, 718 (1993).
- [12] S.Galster *et al.*, Nucl. Phys. **B32**, 221 (1971).
- [13] N.Dombey, Rvw. Mod. Phys. **41**, 236 (1969).

- [14] A.I.Akhiezer and M.P.Rekalo, Sov. J. Part. Nucl. **3**, 277 (1974).
- [15] R.Arnold, C. Carlson, and F.Gross, Phys. Rev. **C23**, 363 (1981).
- [16] B.Blankleider and R.M.Woloshin, Phys. Rev. **C29**, 558 (1984).
- [17] T.Eden *et al.*, Phys. Rev. **C50**, R1749 (1994).
- [18] M.Ostrick *et al.*, Phys. Rev. Lett. **83**, 276 (1999).
- [19] C.Herberg *et al.*, Eur. Phys. J. **A5**, 131 (1999).
- [20] I.Passhier *et al.*, Phys. Rev. Lett. **82**, 4988 (1999).
- [21] D.Rohe *et al.*, Phys. Rev. Lett. **83**, 4257 (1999).
- [22] H.Zhu *et al.*, arXiv:nucl-ex/0105001.
- [23] J.Becker *et al.*, submitted to The Eur. Physical Journal A.
- [24] G.Miller, Phys. Rev. **C66**, 032201 (2001).
- [25] R.Madey and S.Kowalski, spokespeople, Jefferson Lab proposal E93-038.
- [26] D.Day, spokesperson, Jefferson Lab proposal E93-026.
- [27] C.Cioffi degli Atti and S.Scopetta, Phys. Lett. **B404**, 223 (1997).
- [28] R.M.Woloshin, Nucl. Phys. **A496**, 749 (1989).
- [29] J.L.Friar *et al.*, Phys. Rev. **C42**, 2310 (1991).
- [30] C.Cioffi degli Atti, S.Scopetta , E.Pace and G.Salme, Phys. Rev. **C48**, 968 (1993).

- [31] R.W.Schulze and P.U.Sauer, Phys. Rev. **C56** 2293 (1997).
- [32] F.Bissey, A.W.Thomas and I.R. Afnan, Phys. Rev. **C64**, 024004 (2001).
- [33] R.W.Schulze and P.U.Sauer, Phys. Rev. **C48**, 38 (1993).
- [34] W.K.Brooks, spokesperson, Jefferson Lab proposal E94-017.
- [35] A.S.Raskin, T.W.Donnely, Ann. Phys. (N.Y.) **191**, 78 (1989).
- [36] <http://hallaweb.jlab.org/equipment/beam.html>
- [37] <http://hallaweb.jlab.org/physics/experiments/he3/>
- [38] B.Wojtsekhowski, spokesperson, Jefferson Lab proposal E02-013.
- [39] <http://hallaweb.jlab.org/equipment/BigBite/index.html>
- [40] D.J.J.Lange *et al.*, Nucl. Inst. and Meth. **A406**, 182 (1998).
- [41] D.J.J.Lange *et al.*, Nucl. Inst. and Meth. **A412**, 254 (1998).
- [42] H.R.Poolman *et al.*, Nucl. Inst. and Meth. **A314**, 136 (1992).
- [43] <http://www.cst.de/Content/Products/MAFIA/Overview.aspx>
- [44] J.Anand *et al.*, Nucl. Instr. and Meth. **A262**, 329 (1987)
- [45] P.V.Degtyarenko, “Applications of the Photonuclear Fragmentation Model to Radiation Protection Problems”, Proceedings of the Second Specialists’ Meeting on Shielding Aspects of Accelerators, Targets and Irradiation Facilities (SATIF2), 12-13 October 1995, CERN, Geneva, Switzerland.

- [46] B.Wojtsekhowski, P.Degtyarenko, R.Lindgren, “A New Tool for Correlation Studies in Hall A at JLAB, JLab-TN-01-047”, report at the 5th Workshop on Electromagnetically Enduced Two-Hadron Emission, Lund, Sweden, 2001.
- [47] K.Garrow *et al.*, arXiv:hep-ex/0109027.
- [48] Th.Blaich *et al.*, Nucl. Inst. and Meth. **A314**, 136-154 (1992).
- [49] CERN, Geneva, 1993.
- [50] J.B.Birks, *The theory and practice of scintillation counting*, Pergamon Press, 1964.
- [51] W.Leo, *Techniques for Nuclear and Particle Physics Experiments*, Springer Verlag, 1994.
- [52] G.Höhler *et al.*, Nucl. Phys. **B114**, 505 (1976).
- [53] F.Borkowski *et al.*, Z. Phys. **A275**, 29 (1975).
- [54] Y.Nambu, Phys. Rev. **106**, 1366 (1957).
- [55] J.Sakurai, Ann. Phys. (NY) **11**, 1 (1960).
- [56] M.Gari and W.Krüpelmann, Z. Phys. **A322**, 689 (1973); Phys. Lett. **B173**, 10 (1986).
- [57] M.Gari and W.Krüpelmann, Phys. Lett. **B274**, 159 (1992).
- [58] S.Platchkov *et al.*, Nucl. Phys. **A510**, 740 (1990).
- [59] B.Milbrath *et al.*, Phys. Rev. Lett. **80**, 452 (1998); Phys. Rev. Lett. **82**, 2221 (1999).

- [60] A.Chodos *et al.*, Phys. Rev. **D9**, 3471 (1974); Phys. Rev. **D12**, 2733 (1975).
- [61] T.DeGrand *et al.*, Phys. Rev. **D12**, 2060 (1975).
- [62] S.Theberg *et al.*, Phys. Rev. **D22**, 2838 (1980); Can. J. Phys. **60**, 59 (1982).
- [63] A.Gorski, F.Grumer and K.Goeke, Phys. Lett. **B278**, 24 (1992).
- [64] N.Isgur *et al.*, Phys. Rev. **D23**, 163 (1981).
- [65] W. Kohen and H.Weber, Phys. Rev. **D41**, 2201 (1990).
- [66] P.Chung and F.Coester, Phys. Rev. **D44**, 229 (1991).
- [67] M.Ivanov, M.Locher and V.Lyubovitskij, Few-Body System **21**, 131 (1996).
- [68] P.Kroll, M.Schürmann and W.Schweiger, Z. Phys. **338**, 339 (1991).
- [69] R.L.Jaffe, F.E.Close, R.G.Roberts and G.G.Ross, Phys. Lett. **B134**, 449 (1984).
- [70] L.L.Frankfurt and M.I.Strikman, Nucl. Phys. B250, 143 (1985).
- [71] S.Dieterich *et al.*, Phys. Lett. **B500**, 47 (2001).
- [72] J.M.Laget, Phys. Lett. **B273**, 367 (1991).
- [73] C.Ciofi degli Atti, E.Pace, G.Salme, Phys. Rev. **C51**, 1108 (1995).
- [74] L.D.Faddeev, *Mathematical Aspects of the Three-Body Problem*, Daniel Davey and Co.,Inc.,New York, 1965).
- [75] M.M.Sargsian, arXiv:nucl-th/0110053.